

Electronic structure of the cuprate superconducting and pseudogap phases from spectroscopic imaging STM

A R Schmidt^{1,2,3,8}, K Fujita^{1,2,4}, E-A Kim¹, M J Lawler^{1,5},
H Eisaki⁶, S Uchida⁴, D-H Lee³ and J C Davis^{1,2,7}

¹ LASSP, Department of Physics, Cornell University, Ithaca, NY 14853, USA

² Brookhaven National Laboratory, CMPMS Department, Upton, NY 11973, USA

³ Department of Physics, University of California, Berkeley, CA 94720, USA

⁴ Department of Physics, University of Tokyo, Bunkyo-ku, Tokyo 113-0033, Japan

⁵ Department of Physics and Astronomy, Binghamton University, Binghamton, NY 13902, USA

⁶ Institute of Advanced Industrial Science and Technology, Tsukuba, Ibaraki 305-8568, Japan

⁷ School of Physics and Astronomy, University of St. Andrews, Fife KY16 9SS, Scotland

E-mail: andy.schmidt@berkeley.edu

New Journal of Physics **13** (2011) 065014 (32pp)

Received 12 November 2010

Published 21 June 2011

Online at <http://www.njp.org/>

doi:10.1088/1367-2630/13/6/065014

Abstract. We survey the use of spectroscopic imaging scanning tunneling microscopy (SI-STM) to probe the electronic structure of underdoped cuprates. Two distinct classes of electronic states are observed in both the d-wave superconducting (dSC) and the pseudogap (PG) phases. The first class consists of the dispersive Bogoliubov quasiparticle excitations of a homogeneous d-wave superconductor, existing below a lower energy scale $E = \Delta_0$. We find that the Bogoliubov quasiparticle interference (QPI) signatures of delocalized Cooper pairing are restricted to a \mathbf{k} -space arc, which terminates near the lines connecting $\mathbf{k} = \pm(\pi/a_0, 0)$ to $\mathbf{k} = \pm(0, \pi/a_0)$. This arc shrinks continuously with decreasing hole density such that Luttinger's theorem could be satisfied if it represents the front side of a hole-pocket that is bounded behind by the

⁸ Author to whom any correspondence should be addressed.

lines between $\mathbf{k} = \pm(\pi/a_0, 0)$ and $\mathbf{k} = \pm(0, \pi/a_0)$. In both phases, the only broken symmetries detected for the $|E| < \Delta_0$ states are those of a d-wave superconductor. The second class of states occurs proximate to the PG energy scale $E = \Delta_1$. Here the non-dispersive electronic structure breaks the expected 90° -rotational symmetry of electronic structure within each unit cell, at least down to 180° -rotational symmetry. This electronic symmetry breaking was first detected as an electronic inequivalence at the two oxygen sites within each unit cell by using a measure of nematic (C_2) symmetry. Incommensurate non-dispersive conductance modulations, locally breaking both rotational and translational symmetries, coexist with this intra-unit-cell electronic symmetry breaking at $E = \Delta_1$. Their characteristic wavevector \mathbf{Q} is determined by the \mathbf{k} -space points where Bogoliubov QPI terminates and therefore changes continuously with doping. The distinct broken electronic symmetry states (intra-unit-cell and finite \mathbf{Q}) coexisting at $E \sim \Delta_1$ are found to be indistinguishable in the dSC and PG phases. The next challenge for SI-STM studies is to determine the relationship of the $E \sim \Delta_1$ broken symmetry electronic states with the PG phase, and with the $E < \Delta_0$ states associated with Cooper pairing.

Contents

1. Basic electronic structure of hole-doped cuprates	3
1.1. Electronic structure of the superconducting (dSC) and pseudogap (PG) phases .	3
1.2. Two characteristic types of electronic states in underdoped cuprates	3
2. Spectroscopic imaging scanning tunneling microscopy (SI-STM)	6
2.1. Techniques and challenges of SI-STM	6
2.2. Systematic SI-STM studies of $\text{Bi}_2\text{Sr}_2\text{CaCu}_2\text{O}_{8+\delta}$	7
3. Nanoscale electronic disorder in $\text{Bi}_2\text{Sr}_2\text{CaCu}_2\text{O}_{8+\delta}$	7
3.1. Nanoscale electronic disorder of the $E \sim \Delta_1$ PG states	7
3.2. Imaging the effects of interstitial oxygen dopant atoms	9
3.3. Microscopic mechanism of Δ_1 disorder	9
3.4. ‘Kinks’ in $g(E)$ separating homogeneous and heterogeneous states	9
3.5. Summary	10
4. Bogoliubov quasiparticle interference (QPI) imaging	10
4.1. d-Wave BCS Bogoliubov QPI	10
4.2. Summary	11
5. Low-energy excitations of the superconducting phase	11
5.1. Bogoliubov QPI in the dSC phase	11
5.2. Summary	15
6. Low-energy excitations in the PG phase	15
6.1. QPI in a phase-fluctuating d-wave superconductor	15
6.2. Bogoliubov-like QPI in the PG phase	15
6.3. Summary	17

7. Broken spatial symmetries of $E \sim \Delta_1$ states both in the dSC and PG phases	17
7.1. Atomic-scale imaging of the $E \sim \Delta_1$ PG states	17
7.2. Universality of the broken symmetries of the $E \sim \Delta_1$ states	18
7.3. Imaging the broken spatial symmetries of the PG $E \sim \Delta_1$ states	18
7.4. Separating $E \sim \Delta_1$ broken electronic symmetry at intra-unit-cell from that at $\mathbf{Q} = \mathbf{S}_x, \mathbf{S}_y$	20
7.5. Summary	22
8. Overview, conclusions and future	23
8.1. Bipartite electronic structure of underdoped cuprates derived from SI-STM	23
8.2. Microscopic mechanism of intra-unit-cell electronic symmetry breaking	24
8.3. Relationship between the two broken electronic symmetries and the superconductivity	24
8.4. Electronic structure of the cuprate PG phase	26
8.5. Fundamental electronic structure of the hole-doped CuO_2 Mott insulator from SI-STM	26
Acknowledgments	27
References	28

1. Basic electronic structure of hole-doped cuprates

1.1. Electronic structure of the superconducting (dSC) and pseudogap (PG) phases

The electronic structure of the CuO_2 plane is dominated by Cu 3d and O 2p orbitals [1]. Energetically, each Cu $d_{x^2-y^2}$ orbital is split into singly and doubly occupied configurations by on-site Coulomb interactions, with the O p-states intervening. This is a ‘charge-transfer’ [1] Mott insulator that is strongly antiferromagnetic due to superexchange [2, 3]. ‘Hole-doping’ is achieved by removing electrons from the O atoms [4]. This results in the highest-temperature superconductivity available today. The phase diagram [5], with p the number of holes per CuO_2 , is shown schematically in figure 1(a). Antiferromagnetism persists for $p < 2\text{--}5\%$, superconductivity occurs in the range of $5\text{--}10\% < p < 25\text{--}30\%$, and a metallic state exists for $p > 25\text{--}30\%$. The highest superconducting critical temperature T_c always occurs at ‘optimal doping’ near $p \sim 16\%$ and the superconductivity always exhibits d-wave symmetry. With reduced p , an electronic excitation with energy scale $E = \Delta_1$ that is anisotropic in \mathbf{k} -space [5–10] appears at T^* far above the superconducting T_c . This region is labeled the ‘pseudogap’ (PG) phase because Δ_1 could be the energy gap of an ordered phase. Explanations for the PG phase include (i) that it occurs because of effects of a spin-liquid created by hole-doping the antiferromagnetic Mott insulator [3], [11–15], (ii) that it is a phase incoherent d-wave superconductor [16–21] and (iii) that it is an electronic ordered phase [22–36] due to the breaking of electronic symmetries unrelated to superconductivity. Another logically valid possibility is that some combination of these effects is at play. A key challenge for cuprate studies is therefore to achieve a widely accepted understanding of the electronic structure of the PG phase, and to determine its relationship with high-temperature superconductivity.

1.2. Two characteristic types of electronic states in underdoped cuprates

In underdoped cuprates, a variety of different spectroscopies reveal the two energy scales Δ_1 and Δ_0 in association with two distinct types of electronic excited states [5–7], [37–40].

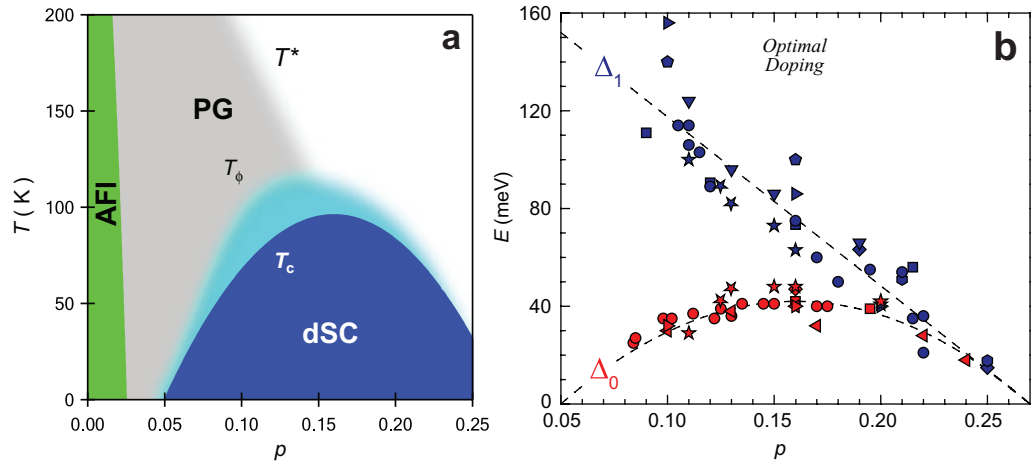


Figure 1. (a) Schematic copper oxide phase diagram. Here, T_c is the critical temperature circumscribing a ‘dome’ of superconductivity, T_ϕ is the maximum temperature at which superconducting phase fluctuations are detectable within the PG phase, and T^* is the approximate temperature at which the PG phenomenology first appears. (b) The two classes of electronic excitations in cuprates. The separation between the energy scales associated with excitations of the superconducting state (dSC, denoted by Δ_0) and those of the PG state (PG, denoted by Δ_1) increases as p decreases (reproduced from [7]). The different symbols correspond to the use of different experimental techniques.

The energies Δ_0 and Δ_1 diverge from one another with diminishing p , as shown in figure 1(b) (reproduced from [7]). Angle-resolved photoemission (ARPES) reveals that, in the PG phase, excitations with $E \sim \Delta_1$ occur in the regions of momentum space near $\mathbf{k} \cong (\pi/a_0, 0); (0, \pi/a_0)$ and that $\Delta_1(p)$ increases rapidly as $p \rightarrow 0$ [6–9]. In contrast, the ‘nodal’ region of \mathbf{k} -space exhibits an ungapped ‘Fermi Arc’ [41] in the PG phase, and a momentum- and temperature-dependent energy gap opens upon this arc in the dSC phase [41–47]. Results from many other spectroscopies appear to be in agreement with this picture. For example, optical transient grating spectroscopy finds that the excitations near Δ_1 propagate very slowly without recombination to form Cooper pairs, whereas lower-energy excitations near the d-wave nodes propagate easily and reform delocalized Cooper pairs as expected [37]. Andreev tunneling exhibits two distinct excitation energy scales that diverge as $p \rightarrow 0$: the first is identified with the PG energy Δ_1 and the second lower scale Δ_0 with the maximum pairing gap energy of delocalized Cooper pairs [38]. Raman spectroscopy finds that scattering near the node is consistent with delocalized Cooper pairing, whereas scattering at the antinodes is not [39]. Finally, muon spin rotation studies of the superfluid density show its evolution to be inconsistent with states on the whole Fermi surface being available for condensation, as if anti-nodal regions cannot contribute to delocalized Cooper pairs [40].

Tunneling density-of-states measurements have reported an energetically particle–hole symmetric excitation energy $E = \pm\Delta_1$, which is indistinguishable in magnitude in the PG and dSC phases [48, 49]. In figure 2(b), we show the evolution of spatially averaged differential tunneling conductance [50–52] $g(E)$ for $\text{Bi}_2\text{Sr}_2\text{CaCu}_2\text{O}_{8+\delta}$. The p dependence of this PG energy $E = \pm\Delta_1$ is indicated by a blue dashed curve (see sections 3, 5 and 7), whereas the approximate

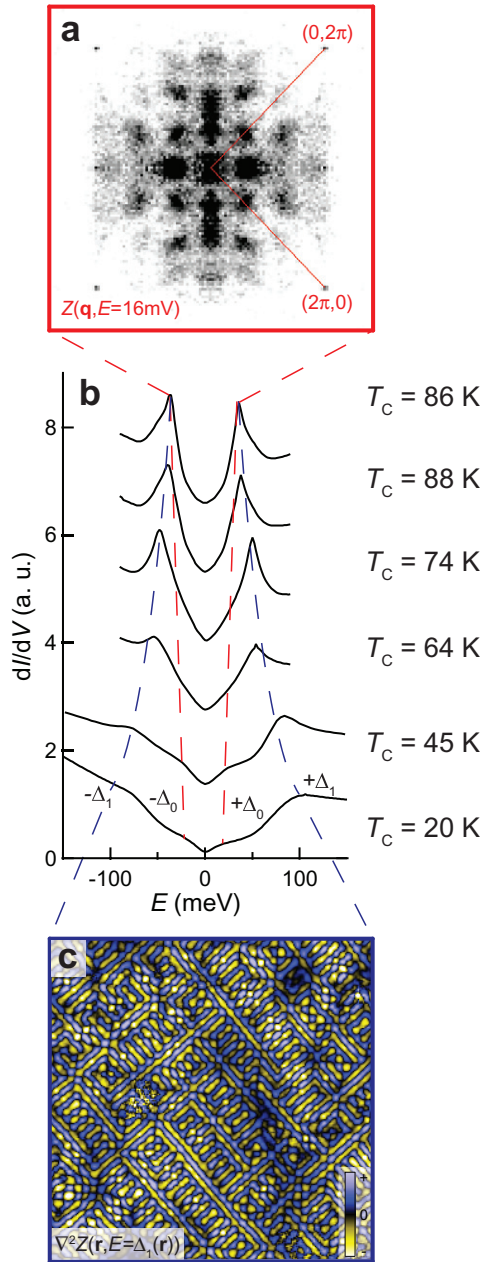


Figure 2. (a) Fourier transform of the conductance ratio map $Z(\mathbf{r}, E)$ at a representative energy below Δ_0 for $T_c = 45$ K $\text{Bi}_2\text{Sr}_2\text{Dy}_{0.2}\text{Ca}_{0.8}\text{Cu}_2\text{O}_{8+\delta}$, which only exhibits the patterns characteristic of homogenous d -wave superconducting quasiparticle interference. (b) Evolution of the spatially averaged tunneling spectra of $\text{Bi}_2\text{Sr}_2\text{CaCu}_2\text{O}_{8+\delta}$ with diminishing p , here characterized by $T_c(p)$. The energies $\Delta_1(p)$ (blue dashed line) are easily detected as the PG edge while the energies $\Delta_0(p)$ (red dashed line) are more subtle but can be identified by the correspondence of the ‘kink’ energy with the extinction energy of Bogoliubov quasiparticles, following the procedures in [54, 58]. (c) Laplacian of the conductance ratio map $Z(\mathbf{r})$ at the PG energy $E = \Delta_1$, emphasizing the local symmetry breaking of these electronic states for strongly underdoped $\text{Ca}_{1.88}\text{Na}_{0.12}\text{CuO}_2\text{Cl}_2$.

p dependence of Δ_0 (as determined from several different tunneling techniques discussed in section 3) is shown by red dashed curves.

The rich spatial complexity of the two classes of electronic states in underdoped cuprates has been exposed more recently by spectroscopic imaging scanning tunneling microscopy. For energies below the weakly doping-dependent [52, 58] lower-scale $E \sim \Delta_0$, the characteristics of dispersive Bogoliubov quasiparticles of a spatially homogeneous superconductor (figure 2(a)) are observed [53–59]. In contrast, the states near $E \sim \Delta_1$ are spatially disordered on the nm scale [50–52], [60–67]. More importantly, when the spatial structure of these non-dispersive states surrounding $E \sim \Delta_1$ is imaged with sub-Angstrom precision, several distinct broken spatial symmetries are observed [50], [57–59], [68] (figure 2(c)). These two classes of excitations also exhibit increasing energy segregation in SI-STM data as $p \rightarrow 0$.

2. Spectroscopic imaging scanning tunneling microscopy (SI-STM)

2.1. Techniques and challenges of SI-STM

Imaging the differential tunneling conductance $dI/dV(\mathbf{r}, E = eV) \equiv g(\mathbf{r}, E = eV)$ with atomic resolution and register, and as a function of both location \mathbf{r} and electron energy E , is referred to as SI-STM. This technique is distinct from other electron spectroscopies in that it can access simultaneously the real space (\mathbf{r} -space) and momentum space (\mathbf{k} -space) electronic structure for both filled and empty states. However, great care must be taken to avoid the serious systematic errors that are endemic to it, especially in the study of underdoped cuprates.

The first systematic problem occurs because the STM tip-sample tunneling current is given by

$$I(\mathbf{r}, z, V) = f(\mathbf{r}, z) \int_0^{eV} N(\mathbf{r}, E) dE, \quad (1)$$

where z is the tip-surface distance, V the tip-sample bias voltage and $N(\mathbf{r}, E)$ the sample's local density of electronic states, while $f(\mathbf{r}, z)$ contains effects of tip elevation and of spatially dependent tunneling matrix elements. The $g(\mathbf{r}, E)$ data are then related to $N(\mathbf{r}, E)$ by [55], [57–59], [60]

$$g(\mathbf{r}, E = eV) = \frac{eI_S}{\int_0^{eV_S} N(\mathbf{r}, E') dE'} N(\mathbf{r}, E), \quad (2)$$

where V_S and I_S are the (constant) junction ‘set-up’ bias voltage and current, respectively. From equation (2), we see that when $\int_0^{eV_S} N(\mathbf{r}, E') dE'$ is strongly heterogeneous at the atomic scale (as it is typically in underdoped cuprates [50–52], [56–68]), $g(\mathbf{r}, E = eV)$ cannot be used to measure $N(\mathbf{r}, E)$. However, for the purposes of measuring distances and spatial symmetries, these potentially severe systematic errors can be canceled [55], [57–59] by using the observable [55]

$$Z(\mathbf{r}, E) \equiv \frac{g(\mathbf{r}, E = +eV)}{g(\mathbf{r}, E = -eV)} = \frac{N(\mathbf{r}, +E)}{N(\mathbf{r}, -E)}, \quad (3)$$

which measures correctly the ratio of the density of states for electron injection to that for extraction at a given \mathbf{r} and E . A related observable that also avoids these systematic errors (but

lacks energy resolution) is [57]

$$R(\mathbf{r}) \equiv \frac{I(\mathbf{r}, E = +eV)}{I(\mathbf{r}, E = -eV)} = \frac{\int_0^{+eV} N(\mathbf{r}, E) dE}{\int_{-eV}^0 N(\mathbf{r}, E) dE}. \quad (4)$$

A different challenge is the random nanoscale variation in $\Delta_1(\mathbf{r})$, which causes the $E \sim \Delta_1$ PG states to be detected at different locations for different bias voltages (figure 3(a)). This problem can be mitigated [58, 68] by scaling the tunnel-bias energy $E = eV$ at each \mathbf{r} by the PG magnitude $\Delta_1(\mathbf{r})$ at the same location. This procedure defines a reduced energy scale $e = E/\Delta_1(\mathbf{r})$ such that

$$Z(\mathbf{r}, e) \equiv Z(\mathbf{r}, E/\Delta_1(\mathbf{r})), \quad (5)$$

in which the $E \sim \Delta_1$ PG states all occur together at $e = 1$ [58].

Another important systematic error has to do with $g(\mathbf{q}, E)$ and $Z(\mathbf{q}, E)$, the Fourier transforms of $g(\mathbf{r}, E)$ and $Z(\mathbf{r}, E)$, respectively. These are used to distinguish any non-dispersive ordering wavevector \mathbf{Q}^* of an electronic ordered phase from the dispersive wavevectors $\mathbf{q}_i(E)$ due to quantum interference patterns of delocalized states. But to achieve sufficient precision in $|\mathbf{q}_i(E)|$ for such discrimination requires that $g(\mathbf{r}, E)$ or $Z(\mathbf{r}, E)$ be measured in large fields of view (FOV) while maintaining atomic resolution and registry, and that the energy resolution be at or below ~ 2 meV. When any smaller FOV or poorer energy resolution is used in $g(\mathbf{r}, E)$ studies, the erroneous impression of non-dispersive modulations is created unavoidably. For $\text{Bi}_2\text{Sr}_2\text{CaCu}_2\text{O}_{8+\delta}$, we have demonstrated both empirically and based on the principles of Fourier transformation that, in both the dSC and PG phases, no deductions distinguishing between dispersive and non-dispersive excitations can be made using Fourier-transformed $g(\mathbf{r}, E)$ data from a FOV smaller than ~ 45 nm square [54, 59].

2.2. Systematic SI-STM studies of $\text{Bi}_2\text{Sr}_2\text{CaCu}_2\text{O}_{8+\delta}$

We have applied these techniques during the sequence of studies summarized herein by measuring $g(\mathbf{r}, E)$ in ~ 45 nm square fields of view in $\text{Bi}_2\text{Sr}_2\text{CaCu}_2\text{O}_{8+\delta}$ samples with $p \cong 0.19, 0.17, 0.14, 0.12, 0.10, 0.08, 0.06$ or with $T_c(\text{K}) = 86, 88, 74, 64, 45, 37, 20$, respectively. Several of these samples were studied in both the dSC and PG phases. Each sample is inserted into the cryogenic ultrahigh vacuum of the SI-STM system, cleaved to reveal an atomically clean BiO surface, and all $g(\mathbf{r}, E)$ measurements were made between 1.9 and 65 K. Three cryogenic SI-STMs (optimized for different purposes) are used throughout these studies. The resulting data set, acquired over approximately a decade, consists of $> 10^8$ atomically resolved and registered tunneling spectra.

3. Nanoscale electronic disorder in $\text{Bi}_2\text{Sr}_2\text{CaCu}_2\text{O}_{8+\delta}$

3.1. Nanoscale electronic disorder of the $E \sim \Delta_1$ PG states

Nanoscale electronic disorder is universal in images of $\Delta_1(\mathbf{r})$ measured on $\text{Bi}_2\text{Sr}_2\text{CaCu}_2\text{O}_{8+\delta}$ samples [50–54], [57–68]. The values of $|\Delta_1|$ ranges from above 130 meV to below 10 meV as the hole density p ranges from 0.06 to 0.22. Highly similar nanoscale electronic disorder is seen in $\text{Bi}_2\text{Sr}_2\text{Cu}_1\text{O}_{6+\delta}$ [56, 65] and in $\text{Bi}_2\text{Sr}_2\text{Ca}_2\text{Cu}_3\text{O}_{10+\delta}$ [69]. In figure 3(a), we show a typical $\text{Bi}_2\text{Sr}_2\text{CaCu}_2\text{O}_{8+\delta}$ $\Delta_1(\mathbf{r})$ image—upon which the sites of the non-stoichiometric

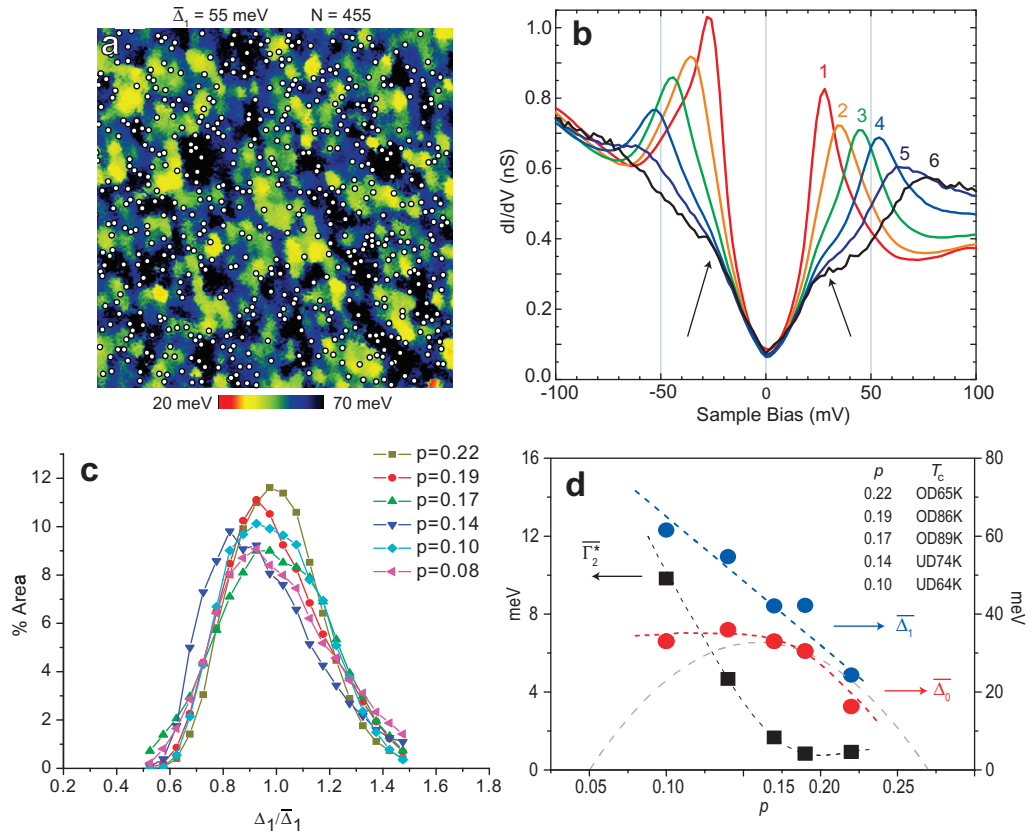


Figure 3. (a) Map of the local energy scale $\Delta_1(\mathbf{r})$ from a 49 nm FOV (corresponding to $\sim 16\,000$ CuO_2 plaquettes) measured on a sample with $T_c = 74$ K. Average gap magnitude $\bar{\Delta}_1$ is at the top, together with the values of N , the total number of dopant impurity states (shown as white circles) detected in the local spectra. (b) The average tunneling spectrum, $g(E)$, associated with each gap value in the field of view in (a). The arrows locate the ‘kinks’ whose energy is Δ_0 . (c) Histograms of equivalent $\Delta_1(\mathbf{r})$ maps from samples with $p = 0.08, 0.10, 0.14, 0.17, 0.19$ and 0.22 normalized to the average Δ_1 in each map. Obviously, these distributions are statistically highly similar. (d) The doping dependence of the average Δ_1 (blue circles), average Δ_0 (red circles) and average antinodal scattering rate Γ_2^* (black squares), each set interconnected by dashed guides to the eye. The higher-scale Δ_1 evolves along the PG line, whereas the lower-scale Δ_0 represents segregation in energy between homogeneous and heterogeneous electronic structure.

oxygen dopant ions are overlaid [51]. Figure 3(b) shows the typical $g(E)$ spectrum associated with each different value of $\pm\Delta_1$ [50]. It also shows how the electronic structure becomes homogeneous [50–56], [58, 59] below a lower energy scale $E = \pm\Delta_0$, as indicated by the arrows. $\text{Bi}_2\text{Sr}_2\text{CuO}_{6+\delta}$ and $\text{Bi}_2\text{Sr}_2\text{Ca}_2\text{Cu}_3\text{O}_{10+\delta}$ samples show similar effects [56, 65, 69]. The distributions of $|\Delta_1|$ measured in units of the spatially averaged $\bar{\Delta}_1$ from six samples with varying hole densities are shown in figure 3(c). As these normalized distributions are virtually independent of p , the microscopic trigger for the Δ_1 -disorder appears universal. Imaging $\Delta_1(\mathbf{r})$

in the PG phase reveals highly similar [59], [64–66] nanoscale electronic disorder. Explaining these Δ_1 -disorder phenomena has been a fascinating challenge.

3.2. *Imaging the effects of interstitial oxygen dopant atoms*

An important element of the explanation is that electron-acceptor atoms must be introduced [70] to generate hole-doped superconductivity from the Mott insulating phase. This almost always creates random distributions of differently charged dopant ions near the CuO_2 planes [71]. The dopant ions in $\text{Bi}_2\text{Sr}_2\text{CaCu}_2\text{O}_{8+\delta}$ are $-2e$ charged interstitials and can conceivably cause a variety of different local effects. For example, electrostatic screening of each ion could accumulate holes at those locations thereby reducing the energy-gap values nearby [72, 73]. Or the dopant ions could generate local crystalline stress/strain [74–78], thereby disordering hopping matrix elements and electron–electron interactions within the unit cell. In $\text{Bi}_2\text{Sr}_2\text{CaCu}_2\text{O}_{8+\delta}$, the locations of interstitial dopant ions can be identified because an atomic scale impurity state occurs at $E = -0.96$ V nearby each ion [51] (figure 3(a)). Strong spatial correlations are observed between the distribution of these impurity states and $\Delta_1(\mathbf{r})$ maps. This implies that dopant ion disorder is responsible for much of the $\Delta_1(\mathbf{r})$ electronic disorder. The primary effect near each dopant ion is a shift in spectral weight from low to high energy with the Δ_1 excitation energy increasing strongly. Moreover, simultaneous imaging of the dopant ion locations and $g(\mathbf{r}, E < \Delta_0)$ reveals that the dispersive $g(\mathbf{r}, E)$ modulations due to scattering of Bogoliubov quasiparticles are well correlated with dopant ion locations, meaning that the dopant ions are an important source of such scattering [50–56] [58, 59] (sections 6 and 7). This demonstration that it is the chemical doping process itself that both disorders Δ_1 and causes strong quasiparticle scattering is of significance because similar nanoscale electronic disorder phenomena are then likely to be common (although with different intensities) in all non-stoichiometric cuprates.

3.3. *Microscopic mechanism of Δ_1 disorder*

The microscopic mechanism of the Δ_1 disorder is not yet fully understood. Hole-accumulation surrounding O^{2-} dopant ions does not appear to be the correct explanation because (i) the modulations in integrated density of filled states are observed to be weak [51] and (ii) Δ_1 is increased nearby the dopant ions [51], a situation diametrically opposite to the expected effect of hole-accumulation there. Atomic substitution at random on the Sr site is known to suppress superconductivity strongly [71], possibly due to geometrical distortions of the unit cell and associated changes in the hopping matrix elements. It has therefore been proposed that the interstitial dopant ions might act similarly, perhaps by displacing the Sr or apical oxygen atoms [71, 74, 75] and thereby distorting the unit cell geometry. Direct support for this point of view comes from the observation that quasi-periodic distortions of the crystal unit-cell geometry yield virtually identical perturbations in $g(E)$ and $\Delta_1(\mathbf{r})$ but now are unrelated to the dopant ions [79]. Thus, it seems that the Δ_1 disorder is not caused primarily by carrier density modulations but by geometrical distortions to the unit cell dimensions with resulting strong local changes in the high-energy electronic structure.

3.4. *‘Kinks’ in $g(E)$ separating homogeneous and heterogeneous states*

So-called ‘kinks’ have been reported ubiquitously in cuprate $g(E)$ spectra [50–52], [55, 56], [58–67]. In general, they are weak perturbations to $N(E)$ near-optimal doping, becoming

clearer as p is diminished [50, 52]. Figure 3(b) demonstrates how, in Δ_1 -sorted $g(E)$ spectra, the kinks are universal but become more obvious for $\Delta_1 > 50$ meV [50, 52]. Each kink can be identified and its energy is labeled $\Delta_0(\mathbf{r})$. By determining $\bar{\Delta}_0$ (the spatial average of $\Delta_0(\mathbf{r})$) as a function of p , we find that this energy $\bar{\Delta}_0$ always divides the electronic structure into two categories [52]. For $E < \bar{\Delta}_0$, the excitations are homogenous in \mathbf{r} -space and well-defined Bogoliubov quasiparticle eigenstates in \mathbf{k} -space (section 6). By contrast, the PG excitations at $E \sim \Delta_1$ are heterogeneous in \mathbf{r} -space and ill defined in \mathbf{k} -space (section 7). Figure 3(d) provides a summary of the evolution of $\bar{\Delta}_0$ and $\bar{\Delta}_1$ with p .

3.5. Summary

The Δ_1 disorder of $\text{Bi}_2\text{Sr}_2\text{CaCu}_2\text{O}_{8+\delta}$ is strongly influenced by the random distribution of dopant ions [51]. This occurs through an electronic process in which geometrical distortions of the crystal unit cell play a prominent role [76–79]. The disorder is strongly reflected in the electronic excitations near the PG energy $E \sim \Delta_1$. The electronic excitations with $E < \Delta_0$, in contrast, are only influenced by the dopant ions via scattering; they are otherwise relatively homogeneous when studied using QPI or by direct imaging [50–52], [61]. As the equivalent $\Delta_1(\mathbf{r})$ disorder is observed in the PG phase, [59], [64–66], [68], an appealing idea has been that these $\Delta_1(\mathbf{r})$ arrangements (figure 3(a)) represent images of the superconducting ‘grains’ of a granular superconductor. However, the superconducting energy gap $\Delta(\mathbf{k})$ when determined using a Bogoliubov quasiparticle interface (QPI) is deduced to be rather spatially homogeneous [50], [53–56], [58, 59]. Moreover, the $E \sim \Delta_1$ PG states exhibit a classic oxygen isotope effect that indicates a strong localized electron–lattice interaction [80]. Finally, atomic resolution imaging of the $E \sim \Delta_1$ states shows them to be non-dispersive and to break several spatial symmetries locally [57–59], [68] (section 7). As none of these latter phenomena are the predicted characteristics of d-wave Bogoliubov quasiparticles within a superconducting grain, it appears implausible at present that $\Delta_1(\mathbf{r})$ represents merely the image of a d-wave granular superconductor.

4. Bogoliubov quasiparticle interference (QPI) imaging

4.1. d-Wave BCS Bogoliubov QPI

Bogoliubov quasiparticles are the excitations generated by breaking Cooper pairs. Bogoliubov QPI occurs when these quasiparticle de Broglie waves are scattered by impurities and the scattered waves undergo quantum interference. In a d-wave cuprate-like superconductor with a single hole-like band of uncorrelated electrons, the Bogoliubov quasiparticle dispersion $E(\mathbf{k})$ would have ‘banana-shaped’ constant energy contours. For a given energy E , the d-symmetry of the superconducting energy gap would then cause strong maxima to appear in the joint-density-of-states at the eight tips $\mathbf{k}_j(E)$; $j = 1, 2, \dots, 8$ of these ‘bananas’. Elastic scattering between the $\mathbf{k}_j(E)$ then produces \mathbf{r} -space interference patterns in the local-density-of-states $N(\mathbf{r}, E)$. The resulting $g(\mathbf{r}, E)$ modulations detectable by SI-STM should exhibit $16 \pm \mathbf{q}$ pairs of dispersive wavevectors in $g(\mathbf{q}, E)$ (figure 4(a)). The set of these wavevectors that is specifically characteristic of d-wave superconductivity consists of seven: $\mathbf{q}_i(E)$ $i = 1, \dots, 7$ with $\mathbf{q}_i(-E) = \mathbf{q}_i(+E)$. This is the so-called ‘octet model’ [81–83] within which, by using the point-group symmetry of the first CuO_2 Brillouin zone, the locus of the above-mentioned

tips at $\mathbf{k}_B(E) = (k_x(E), k_y(E))$ is determined from

$$\begin{aligned} \mathbf{q}_1 &= (2k_x, 0), & \mathbf{q}_4 &= (2k_x, 2k_y), & \mathbf{q}_7 &= (k_x - k_y, k_y - k_x), \\ \mathbf{q}_2 &= (k_x + k_y, k_y - k_x), & \mathbf{q}_5 &= (0, 2k_y), \\ \mathbf{q}_3 &= (k_x + k_y, k_y + k_x), & \mathbf{q}_6 &= (k_x - k_y, k_y + k_x). \end{aligned} \quad (6)$$

When these $\mathbf{q}_i(E)$ are measured from $Z(\mathbf{q}, E)$, the Fourier transform of spatial modulations seen in $Z(\mathbf{r}, E)$ (see figure 2(a), for example), the $\mathbf{k}_B(E)$ can then be determined by using equation (6) within the requirement that all of its independent solutions are consistent at all energies. The superconductor's Cooper-pairing energy gap $\Delta(\mathbf{k})$ is then determined directly by inverting $\mathbf{k}_B(E = \Delta)$. In $\text{Bi}_2\text{Sr}_2\text{CaCu}_2\text{O}_{8+\delta}$ near-optimal doping, measurements from QPI of the Fermi surface location $\mathbf{k}_B(E)$, and of the superconducting $\Delta(\mathbf{k})$ (figure 4(b)), are consistent with ARPES [54, 84]. Both in $\text{Ca}_{2-x}\text{Na}_x\text{CuO}_2\text{Cl}_2$ and $\text{Bi}_2\text{Sr}_2\text{CaCu}_2\text{O}_{8+\delta}$, the QPI octet model yields $\mathbf{k}_B(E)$ and $\Delta(\mathbf{k})$ equally well [55, 56]. Moreover, the basic validity of the fundamental \mathbf{k} -space phenomenology behind the d-wave QPI ‘octet’ model has been confirmed by ARPES studies [85–87].

4.2. Summary

Fourier transformation of $Z(\mathbf{r}, E)$ in combination with the octet model of d-wave BCS Bogoliubov QPI yields the two branches of the Bogoliubov excitation spectrum $\mathbf{k}_B(\pm E)$ plus the superconducting energy gap magnitude $\pm\Delta(\mathbf{k})$ along the specific \mathbf{k} -space trajectory \mathbf{k}_B for both filled and empty states in a single experiment. As only the Bogoliubov states of a d-wave superconductor could exhibit such a set of 16 pairs of interference wavevectors with $\mathbf{q}_i(-E) = \mathbf{q}_i(+E)$ and all dispersions internally consistent within the octet model, the energy gap $\pm\Delta(\mathbf{k})$ determined by these procedures is definitely that of the delocalized Cooper pairs.

5. Low-energy excitations of the superconducting phase

5.1. Bogoliubov QPI in the dSC phase

Bogoliubov QPI imaging techniques have been used to study the evolution of \mathbf{k} -space electronic structure with falling p in $\text{Bi}_2\text{Sr}_2\text{CaCu}_2\text{O}_{8+\delta}$. In the SC phase, the expected 16 pairs of \mathbf{q} -vectors are always observed in $Z(\mathbf{q}, E)$ and are found consistent with each other within the octet model (figures 2(a) and 4(c)). Remarkably, however, we find that in underdoped $\text{Bi}_2\text{Sr}_2\text{CaCu}_2\text{O}_{8+\delta}$, the dispersion of octet model \mathbf{q} -vectors always stops at the same weakly doping-dependent [50, 56, 58] excitation energy Δ_0 and at \mathbf{q} -vectors indicating that the relevant \mathbf{k} -space states are still far from the boundary of the Brillouin zone. These observations are quite unexpected in the context of the d-wave BCS octet model. Moreover, for $E > \Delta_0$, the dispersive octet of \mathbf{q} -vectors disappears and we observe three non-dispersive \mathbf{q} -vectors: the reciprocal lattice vector \mathbf{Q} along with \mathbf{q}_1^* and \mathbf{q}_5^* (see figure 4(c)). The equivalent pair of non-dispersive wavevectors to \mathbf{q}_1^* and \mathbf{q}_5^* has also been detected by SI-STM in $\text{Ca}_{2-x}\text{Na}_x\text{CuO}_2\text{Cl}_2$ [42] and $\text{Bi}_2\text{Sr}_2\text{Cu}_1\text{O}_{6+\delta}$ [56], and by ARPES in $\text{Ca}_{2-x}\text{Na}_x\text{CuO}_2\text{Cl}_2$ [42] and $\text{Bi}_2\text{Sr}_2\text{CaCu}_2\text{O}_{8+\delta}$ [86, 87].

By using the QPI imaging techniques described in section 4, we show in figure 4(d) the locus of Bogoliubov quasiparticle states $\mathbf{k}_B(E)$ determined as a function of p . Here we see that when the Bogoliubov QPI patterns disappear at Δ_0 , the \mathbf{k} -states are near the diagonal lines between $\mathbf{k} = (0, \pi/a_0)$ and $\mathbf{k} = (\pi/a_0, 0)$ within the CuO_2 Brillouin zone. These

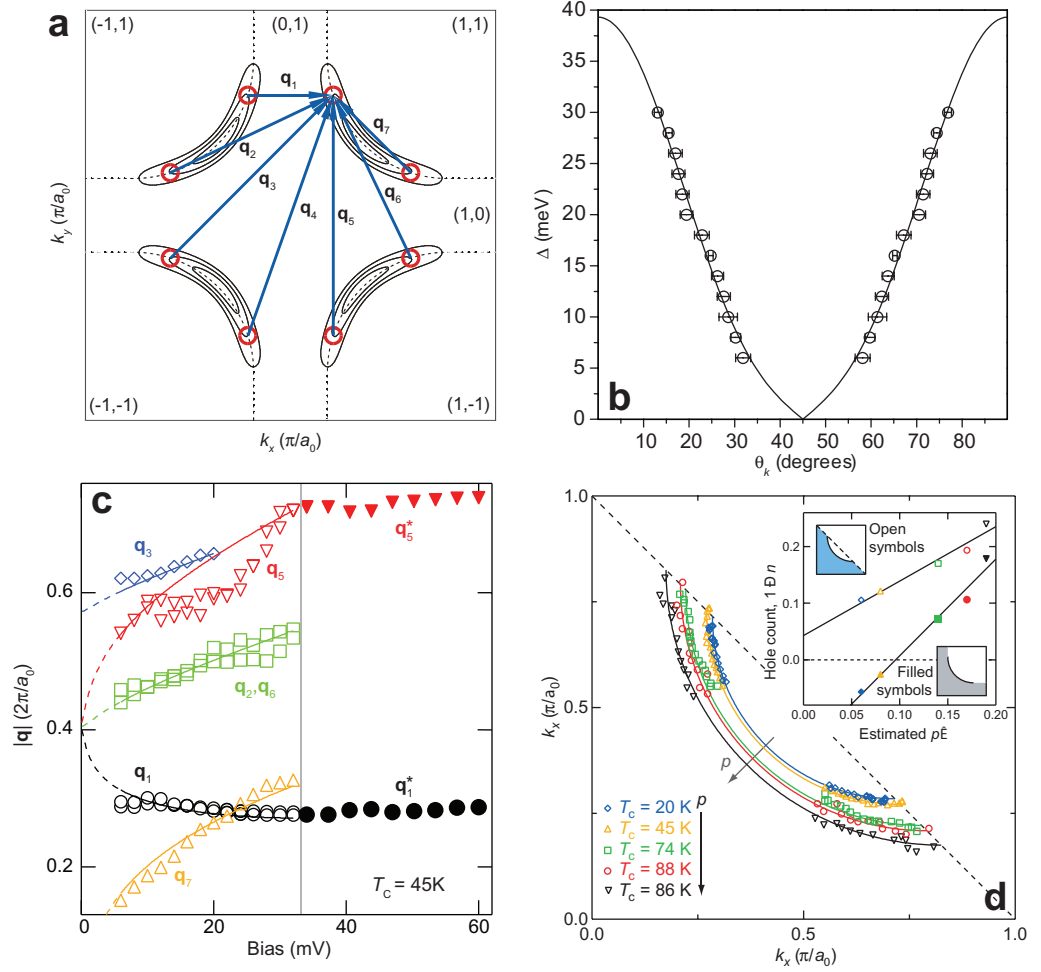


Figure 4. (a) The expected wavevectors of quasiparticle interference patterns in a superconductor with an electronic band structure like that of $\text{Bi}_2\text{Sr}_2\text{CaCu}_2\text{O}_{8+\delta}$. Solid lines indicate the \mathbf{k} -space locations of several banana-shaped quasiparticle contours of constant energy as they increase in size with increasing energy. As an example, at a specific energy, the octet of regions of high JDOS are shown as red circles. The seven primary scattering \mathbf{q} -vectors interconnecting elements of the octet are shown in blue. (b) A plot of the superconducting energy gap $\Delta(\theta_k)$ determined from octet model inversion of QPI measurements, shown as open circles [54]. These were extracted using the measured position of scattering vectors \mathbf{q}_1 through \mathbf{q}_7 . The solid line is a fit to the data. The mean value of Δ_1 for this overdoped $T_c = 86$ K sample was 39 meV. (c) The magnitude of various extracted QPI vectors, plotted as a function of energy. Whereas the expected energy dispersion of the octet vectors $\mathbf{q}_i(E)$ is apparent for $|E| < 32$ mV, the peaks that avoid extinction (\mathbf{q}_1^* and \mathbf{q}_5^*) always become non-dispersive above Δ_0 (vertical gray line). (d) Locus of the Bogoliubov band minimum $\mathbf{k}_B(E)$ found from extracted QPI peak locations $\mathbf{q}_i(E)$, in five independent $\text{Bi}_2\text{Sr}_2\text{CaCu}_2\text{O}_{8+\delta}$ samples with decreasing hole density. Fits to quarter-circles are shown and, as p decreases, these curves enclose a progressively smaller area. The BQP interference patterns disappear near the perimeter of a \mathbf{k} -space region bounded

Figure 4. (Continued) by the lines joining $\mathbf{k} = (0, \pm\pi/a_0)$ and $\mathbf{k} = (\pm\pi/a_0, 0)$. The spectral weights of \mathbf{q}_2 , \mathbf{q}_3 , \mathbf{q}_6 and \mathbf{q}_7 vanish at the same place (dashed line; see also [58]). Filled symbols in the inset represent the hole count $p = 1 - n$ derived using the simple Luttinger theorem, with the fits to a large, hole-like Fermi surface indicated schematically here in gray. Open symbols in the inset are the hole counts calculated using the area enclosed by the Bogoliubov arc and the lines joining $\mathbf{k} = (0, \pm\pi/a_0)$ and $\mathbf{k} = (\pm\pi/a_0, 0)$, and are indicated schematically here in blue.

\mathbf{k} -space Bogoliubov arc tips are defined both by the change from dispersive to non-dispersive characteristics and the disappearance of the \mathbf{q}_2 , \mathbf{q}_3 , \mathbf{q}_6 and \mathbf{q}_7 modulations (see figure 4(c)). Thus, the signature of delocalized Cooper pairing is confined to an arc (fine solid lines in figure 4(d)), and this arc shrinks with falling p [58]. This discovery has been supported directly by angle-resolved photoemission studies [40, 47] and by SI-STM studies of $\text{Ca}_{2-x}\text{Na}_x\text{CuO}_2\text{Cl}_2$ [55] and $\text{Bi}_2\text{Sr}_2\text{Cu}_1\text{O}_{6+\delta}$ [56], and indirectly by analyses of $g(\mathbf{r}, E)$ by fitting to a multi-parameter model for \mathbf{k} -space structure in the presence of a dSC energy gap [67].

The minima (maxima) of the Bogoliubov bands $\mathbf{k}_B(\pm E)$ should occur at the \mathbf{k} -space location of the Fermi surface of the non-superconducting state. One can therefore ask if the carrier-density count satisfies Luttinger's theorem, which states that twice the \mathbf{k} -space area enclosed by the Fermi surface, measured in units of the area of the first Brillouin zone, equals the number of electrons per unit cell, n . In figure 4(d), we show as fine solid lines hole-like Fermi surfaces fitted to our measured $\mathbf{k}_B(E)$. Using Luttinger's theorem with these \mathbf{k} -space contours extended to the zone face would result in a calculated hole density p for comparison with the estimated hole density in the samples. These data are shown by filled symbols in the inset to figure 4(d). We see that Luttinger theorem is strongly violated at all doping below $p \sim 10\%$. However, Luttinger theorem can, in principle, be amended in a doped Mott insulator [58] so that the zero-energy contours bounding the region representing carriers are defined, not only by poles in Green's functions, but also by their zeros [88]. The locus of zeros of these Green's functions might be expected to occur at the lines joining $\mathbf{k} = (0, \pi/a_0)$ to $\mathbf{k} = (\pi/a_0, 0)$. In that situation, the hole density is related quantitatively to the area between the $\mathbf{k} = (0, \pm\pi/a_0)$ – $\mathbf{k} = (\pi/a_0, 0)$ lines and the arcs. The carrier densities calculated in this fashion are shown by open symbols in the inset to figure 4(d) and are obviously in much better agreement with the chemical hole density.

Figure 5 provides a doping-dependence analysis of the locations of the ends of the arc-tips at which Bogoliubov QPI signature disappears and where the \mathbf{q}_1^* and \mathbf{q}_5^* non-dispersive modulations appear. Figure 5(a) shows a typical $Z(\mathbf{q}, E)$ for which $\Delta_0 < E < \Delta_1$. Here the vectors \mathbf{q}_1^* and \mathbf{q}_5^* (see figure 4(c)) are labeled along with the Bragg vectors \mathbf{Q}_x and \mathbf{Q}_y . Figure 5(b) shows a schematic representation of the arc of the \mathbf{k} -space supporting Bogoliubov QPI in blue. We show below how its termination points on the lines linking $\mathbf{k} = \pm(0, \pi/a_0)$ and $\mathbf{k} = \pm(\pi/a_0, 0)$ directly link the \mathbf{q}_1^* and \mathbf{q}_5^* wavevectors to the CuO_2 Brillouin zone size (via the arrows in red). Figure 5(c) shows the doping dependence for $\text{Bi}_2\text{Sr}_2\text{CaCu}_2\text{O}_{8+\delta}$ of the location of both \mathbf{q}_1^* and \mathbf{q}_5^* measured from $Z(\mathbf{q}, E)$ [58]. The measured magnitude of \mathbf{q}_1^* and \mathbf{q}_5^* versus p are then shown in figure 5(d) along with the sum $\mathbf{q}_1^* + \mathbf{q}_5^*$, which is always equal to 2π . This demonstrates that, as the Bogoliubov QPI extinction point travels along the

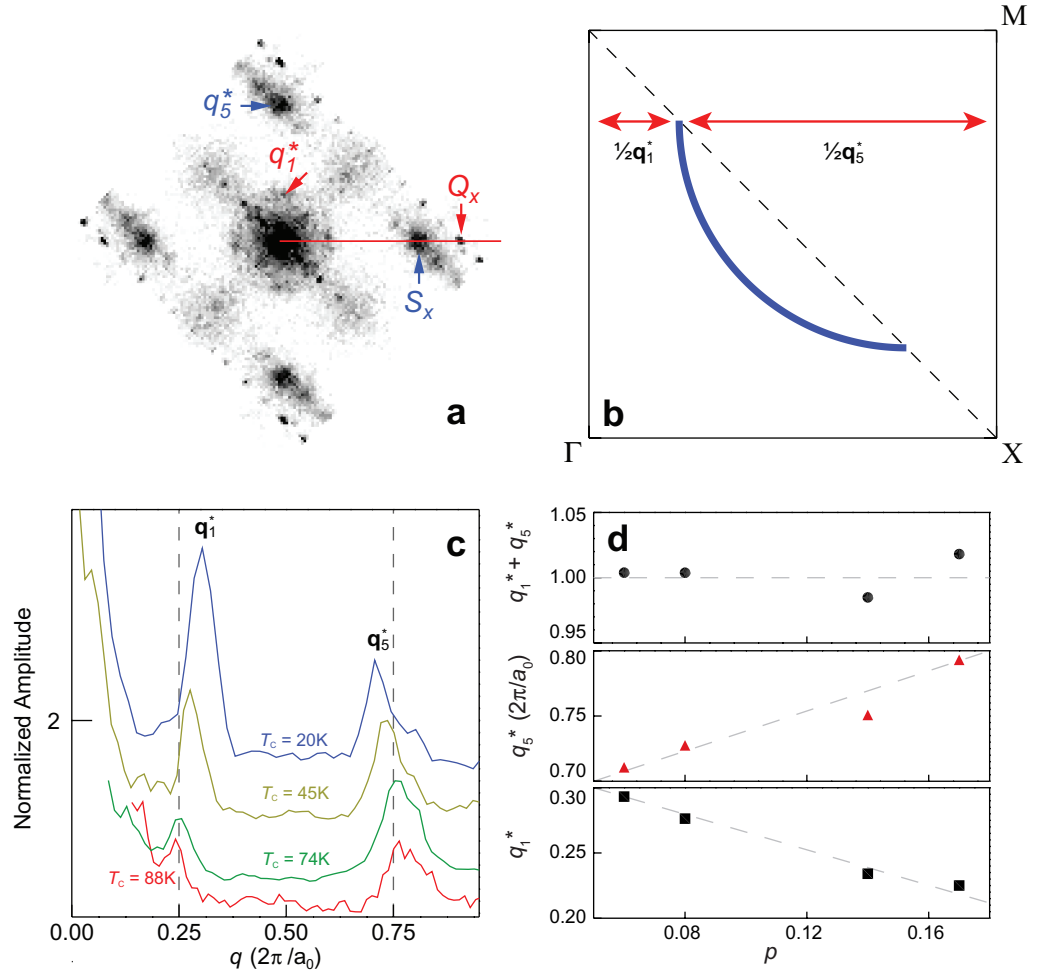


Figure 5. (a) Fourier transform of the conductance ratio $Z(\mathbf{q}, E = 48 \text{ meV})$ at a representative energy between Δ_0 and Δ_1 for underdoped $T_c = 74 \text{ K}$ $\text{Bi}_2\text{Sr}_2\text{CaCu}_2\text{O}_{8+\delta}$. The red line schematically indicates the source of the data in (c). The arrows label the location of the wavevectors \mathbf{q}_1^* , \mathbf{q}_5^* , \mathbf{S}_x and \mathbf{Q}_x described in the text. (b) Schematic diagram of the Brillouin zone illustrating the relationship of non-dispersive \mathbf{q}_1^* and \mathbf{q}_5^* to the ends of the Bogoliubov arc. (c) Doping dependence of line-cuts of $Z(\mathbf{q}, E = 48 \text{ meV})$ extracted along the Cu–O bond direction \mathbf{Q}_x . The vertical dashed lines demonstrate that the non-dispersive \mathbf{q} -vectors at energies between Δ_0 and Δ_1 are not commensurate harmonics of a $4a_0$ periodic modulation, but instead evolve in a fashion directly related to the extinction point of the Fermi arc. The data in (c) have been normalized to the peak amplitude of \mathbf{q}_5^* and offset vertically for clarity. (d) \mathbf{q}_1^* , \mathbf{q}_5^* and their sum $\mathbf{q}_1^* + \mathbf{q}_5^*$ as a function of p demonstrating that individually these modulations evolve with doping, while their sum does not change and is equal to the reciprocal lattice vector defining the first Brillouin zone.

line from $\mathbf{k} = (0, \pi/a_0)$ and $\mathbf{k} = (\pi/a_0, 0)$ ([58] and figures 4(d) and 5(b)), the wavelengths of incommensurate modulations \mathbf{q}_1^* and \mathbf{q}_5^* are controlled by its \mathbf{k} -space location [58]. Equivalent phenomena have also been reported for $\text{Bi}_2\text{Sr}_2\text{CuO}_{6+\delta}$ [56].

5.2. Summary

Because the superconducting $\Delta(\mathbf{k})$ must be translationally invariant for Bogoliubov QPI to exhibit the observed \sim long-range interference patterns, cuprate superconductivity is found to be rather spatially homogeneous (as implied also by direct $g(E)$ spectra studies [50, 67]). When p is reduced, the Bogoliubov QPI signature of which \mathbf{k} -space states contribute to Cooper pairing is confined to an arc [50, 54, 56, 58] in \mathbf{k} -space that shrinks with falling doping. The arc tips lie near the diagonal lines connecting $\mathbf{k} = (0, \pm\pi/a_0)$ and $\mathbf{k} = (\pm\pi/a_0, 0)$ and occur at a weakly doping-dependent [52, 58] energy $E = \Delta_0$ that is indistinguishable from (i) where the $g(E)$ kinks occur [52] and (ii) where electronic homogeneity is lost [50, 56], [58–61]. The shrinking of this arc with decreasing hole density could satisfy Luttinger's theorem if it is actually the front side of a hole pocket bounded behind by the $\mathbf{k} = (0, \pm\pi/a_0)$ – $\mathbf{k} = (\pm\pi/a_0, 0)$ lines. We find that the gap energy at the arc tip Δ_0 is associated with the disappearance of the QPI signature of delocalized Cooper pairs for $E \geq \Delta_0$ (and simultaneously also the loss of electronic homogeneity and the kink in the density of states), while the upper energy Δ_1 is associated with an apparently quite distinct \mathbf{r} -space electronic structure of the $E \sim \Delta_1$ PG excitations (section 7). Finally, the wavelengths of incommensurate modulations \mathbf{q}_1^* and \mathbf{q}_5^* are controlled by the \mathbf{k} -space locations at which the Bogoliubov QPI signatures disappear, and these points evolve continuously with doping along the line joining $\mathbf{k} = (0, \pm\pi/a_0)$ – $\mathbf{k} = (\pm\pi/a_0, 0)$. This appears to rule out the interpretation of these non-dispersive conductance modulations as being due to local charge organization in real space.

6. Low-energy excitations in the PG phase

6.1. QPI in a phase-fluctuating d-wave superconductor

Because cuprate superconductivity is quasi-two-dimensional, the superfluid density increases from zero approximately linearly with p , and the superconducting energy gap $\Delta(\mathbf{k})$ exhibits four \mathbf{k} -space nodes, fluctuations in the quantum phase $\phi(\mathbf{r}, t)$ of the superconducting order parameter $\Psi = \Delta(\mathbf{k})e^{i\phi(\mathbf{r}, t)}$ could have strong effects on the superconductivity at low hole density [16–21]. Phenomena indicative of phase fluctuating superconductivity are detectable for cuprates in particular regions of the phase diagram [89–94], as indicated schematically by the region $T_c < T < T_\phi$ (figure 1(a)). The techniques involved include terahertz transport studies [89], the Nernst effect [90, 91], torque-magnetometry measurements [92], field dependence of the diamagnetism [93] and zero-bias conductance enhancement [94].

A spectroscopic signature of phase-incoherent d-wave superconductivity in the PG phase could be the continued existence of the Bogoliubov-like QPI octet, as described in the previous two sections. This is because, if the quantum phase $\phi(\mathbf{r}, t)$ is fluctuating while the energy gap magnitude $\Delta(\mathbf{k})$ remains largely unchanged, the particle–hole symmetric octet of high joint-density-of-states regions generating the QPI should continue to exist [95–97]. However, any gapped \mathbf{k} -space regions supporting Bogoliubov-like QPI in the PG phase must then occur beyond the tips of the ungapped Fermi Arc [41].

6.2. Bogoliubov-like QPI in the PG phase

The temperature evolution of the Bogoliubov octet in $Z(\mathbf{q}, E)$ was studied as a function of increasing temperature from the dSC phase into the PG phase using a 48 nm square FOV

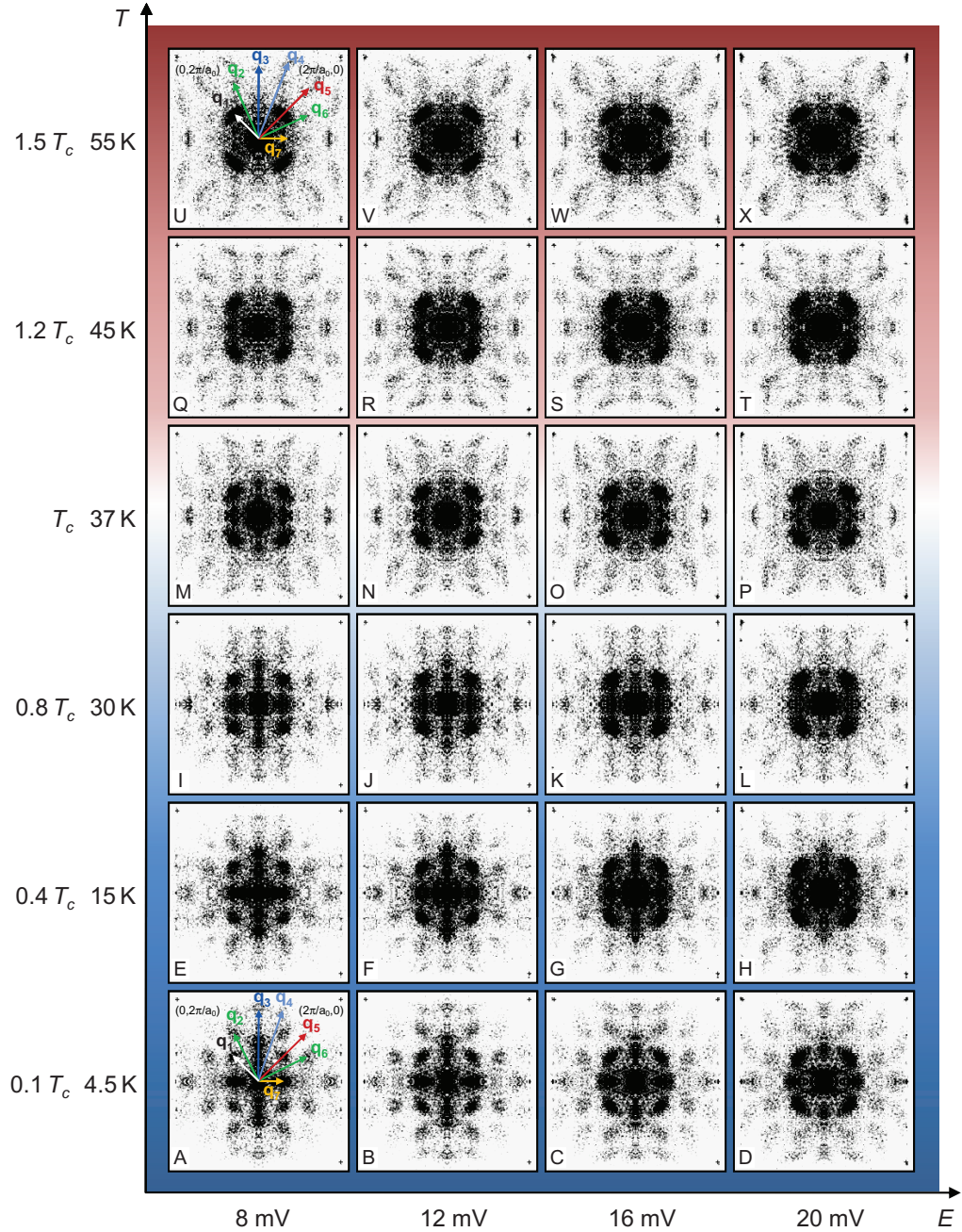


Figure 6. (a–x) Differential conductance maps $g(\mathbf{r}, E)$ were obtained from the same sample in an atomically resolved and registered FOV $>45 \times 45 \text{ nm}^2$ at six temperatures. Each panel shown is the Fourier transform $Z(\mathbf{q}, E)$ of $Z(\mathbf{r}, E) \equiv g(\mathbf{r}, +E)/g(\mathbf{r}, -E)$ for a given energy and temperature. The QPI signals evolve dispersively with energy along the horizontal energy axis. The temperature dependence of QPI for a given energy evolves along the vertical axis. The octet-model set of QPI wave vectors is observed for every E and T as seen, for example, by comparing (a) and (u), each of which has the labeled octet vectors. Within the basic octet QPI phenomenology, there is no particular indication in these data of where the superconducting transition T_c , as determined by resistance measurements, occurs.

and with sub-unit-cell resolution. Representative $Z(\mathbf{q}, E)$ for six temperatures are shown in figure 6; the $\mathbf{q}_i(E)$ ($i = 1, 2, \dots, 7$) characteristic of the superconducting octet model are observed to remain unchanged upon passing above T_c to at least $T \sim 1.5T_c$. This demonstrates that the Bogoliubov-like QPI octet phenomenology exists in the cuprate PG phase (although it is generated by different regions of \mathbf{k} -space, and thus different $\Delta(\mathbf{k})$, than in the same sample in the SC phase). Thus, for the low-energy ($E < 35$ mV) excitations in the underdoped PG phase, the $\mathbf{q}_i(E)$ ($i = 1, 2, \dots, 7$) characteristic of the octet model are preserved unchanged upon passing above T_c . Importantly, all seven $\mathbf{q}_i(E)$ ($i = 1, 2, \dots, 7$) modulation wavevectors, which are dispersive in the dSC phase, remain dispersive into the PG phase still consistent with the octet model [59]. The octet wavevectors also retain their particle-hole symmetry $\mathbf{q}_i(+E) = \mathbf{q}_i(-E)$ in the PG phase and the $g(\mathbf{r}, E)$ modulations occur in the same energy range and emanate from the same contour in \mathbf{k} -space as those observed at lowest temperatures [59]. However, with increasing T , the particle-hole symmetric energy gap $\Delta(\mathbf{k})$ closes near the nodes, leaving behind a growing Fermi arc of gapless excitations (section 8.1).

6.3. Summary

All of the Bogoliubov QPI signatures detectable in the dSC phase survive virtually unchanged into the underdoped PG phase—up to at least $T \sim 1.5T_c$ for strongly underdoped $\text{Bi}_2\text{Sr}_2\text{CaCu}_2\text{O}_{8+\delta}$ samples. Moreover, for $E < \Delta_0$, all seven dispersive $\mathbf{q}_i(E)$ modulations characteristic of the octet model in the dSC phase remain dispersive in the PG phase. These observations rule out the existence for all $E \leq \Delta_0$ of non-dispersive $g(E)$ modulations at finite ordering wavevector \mathbf{Q}^* , which would be indicative of a static electronic order (breaking translational symmetry). This conclusion is in agreement with the results of ARPES studies [85, 86]. Instead, the observed excitations are indistinguishable from the dispersive \mathbf{k} -space eigenstates of a phase incoherent d-wave superconductor [59]. Thus, the SI-STM picture of electronic structure in the strongly underdoped PG phase actually contains three elements: (i) the ungapped Fermi arc [41], (ii) the particle-hole symmetric gap $\Delta(\mathbf{k})$ of a phase incoherent superconductor [59] and (iii) the non-dispersive and locally symmetry breaking excitations at the $E \sim \Delta_1$ energy scale [50], [57–59], [68] (which remain completely unaltered upon the transition between the dSC and the PG phases [59, 68]). This three-component description of the electronic structure of the cuprate PG phase (figure 10(d)) has recently been confirmed in detail by ARPES studies [98].

7. Broken spatial symmetries of $E \sim \Delta_1$ states both in the dSC and PG phases

7.1. Atomic-scale imaging of the $E \sim \Delta_1$ PG states

In general, for underdoped cuprates, the electronic excitations in the PG energy range $E \sim \Delta_1$ are observed to be highly anomalous. They are associated with a strong antinodal PG in \mathbf{k} -space [8, 9], they exhibit slow dynamics without recombination to form Cooper pairs [37], their Raman characteristics appear distinct from expectations for a d-wave superconductor [39] and they appear not to contribute to superfluid density [40].

As described in sections 5 and 6, underdoped cuprates exhibit an octet of dispersive Bogoliubov QPI wavevectors $\mathbf{q}_i(E)$, but only upon a limited and doping-dependent arc in \mathbf{k} -space. But these effects always disappear above $E \cong \Delta_0$ to be replaced by a spectrum of non-dispersive states [50], [56–59], [68] surrounding the PG-energy $E \sim \Delta_1$ (figure 4(c)). The

$Z(\mathbf{q}, E > \Delta_0)$ modulations exhibit the two non-dispersive \mathbf{q} -vectors, \mathbf{q}_1^* and \mathbf{q}_5^* , which evolve with p , as shown in figure 5. The \mathbf{q}_1^* modulations appear as the energy transitions from below to above Δ_0 but disappear quickly, leaving only two primary electronic structure elements of the PG -energy electronic structure in $Z(\mathbf{q}, E \cong \Delta_1)$. These occur at $\mathbf{Q}_x = (1, 0)2\pi/a_0$ and $\mathbf{Q}_y = (0, 1)\pi/a_0$, which are the Bragg peaks representing the periodicity of the unit cell, and at $\mathbf{S}_x \equiv (\sim 3/4, 0)2\pi/a_0$, $\mathbf{S}_y \equiv (0, \sim 3/4)2\pi/a_0$, which are due to the local breaking of lattice translation symmetry at the nanoscale. The doping evolution of $|\mathbf{S}_x| = |\mathbf{S}_y|$ (which is by definition that of \mathbf{q}_5^* -see figure 5), as shown in figure 5(d), indicates that these incommensurate modulations are linked to the doping dependence of the extinction point of the arc of Bogoliubov QPI.

Atomically resolved \mathbf{r} -space images of the static phenomena in $Z(\mathbf{r}, E)$ show highly similar spatial patterns at all energies near Δ_1 but with variations in intensity due to the Δ_1 disorder (figure 3(a)). By changing to reduced energy variables $e(\mathbf{r}) = E/\Delta_1(\mathbf{r})$ and imaging $Z(\mathbf{r}, e)$, it becomes clear that these modulations exhibit a strong maximum in intensity at $e = 1$. This is demonstrated directly in figure 7, where the relative intensity of the modulations (all in the same units and contrast scales) exhibits a strong maximum at $e = 1$ [58]. Thus, the PG states of underdoped cuprates locally break translational symmetry, and reduce the expected 90° -rotational (C_4) symmetry of states within the unit cell to at least 180° -rotational (C_2) symmetry [57–59], and possibly to an even lower symmetry.

7.2. Universality of the broken symmetries of the $E \sim \Delta_1$ states

Theoretical concerns have been advanced about such spatial structuring of the cuprate PG states, including the possibility of spurious rotation symmetry breaking due to the dopant atoms [99]. To address such issues, we carried out a sequence of identical experiments on two radically different cuprates at the same p : strongly underdoped $\text{Ca}_{1.88}\text{Na}_{0.12}\text{CuO}_2\text{Cl}_2$ (Na-CCOC; $T_c \sim 21$ K) and $\text{Bi}_2\text{Sr}_2\text{Dy}_{0.2}\text{Ca}_{0.8}\text{Cu}_2\text{O}_{8+\delta}$ (Dy-Bi2212; $T_c \sim 45$ K). These materials have completely different crystallographic structures, chemical constituents, dopant-ion species and inequivalent dopant-ion sites within the crystal-termination layers lying between the CuO_2 plane and the STM tip [57]. However, images of the $E \sim \Delta_1$ PG states for these two systems demonstrate virtually indistinguishable electronic structure arrangements [57]. Obviously, these symmetry-breaking effects within every CuO_2 unit cell [57, 68] cannot be governed by individual dopant ions because there is only a single such ion for every ~ 20 planar oxygen atoms in Dy-Bi2212. Moreover, the dopant ions occur at quite different locations (substitutional/interstitial, respectively) in the unit cells of Na-CCOC and Dy-Bi2212. Thus, the virtually identical phenomena in images of the atomic-scale-broken symmetries $E \sim \Delta_1$ PG states in Na-CCOC and Dy-Bi2212 must occur due to the only common characteristic of these two radically different materials. Therefore, $Z(\mathbf{r}, e = 1)$ images of the spatial structure of the cuprate PG states [57–59], [68] should be ascribed to the intrinsic electronic structure of the CuO_2 plane.

7.3. Imaging the broken spatial symmetries of the PG $E \sim \Delta_1$ states

To explore which spatial symmetries are actually broken by the cuprate PG states, we use sub-unit-cell resolution $Z(\mathbf{r}, e)$ imaging performed on multiple different underdoped $\text{Bi}_2\text{Sr}_2\text{CaCu}_2\text{O}_{8+\delta}$ samples with T_c s between 20 and 55 K. The necessary registry of the Cu sites in each $Z(\mathbf{r}, e)$ is achieved by a picometer scale transformation that renders the

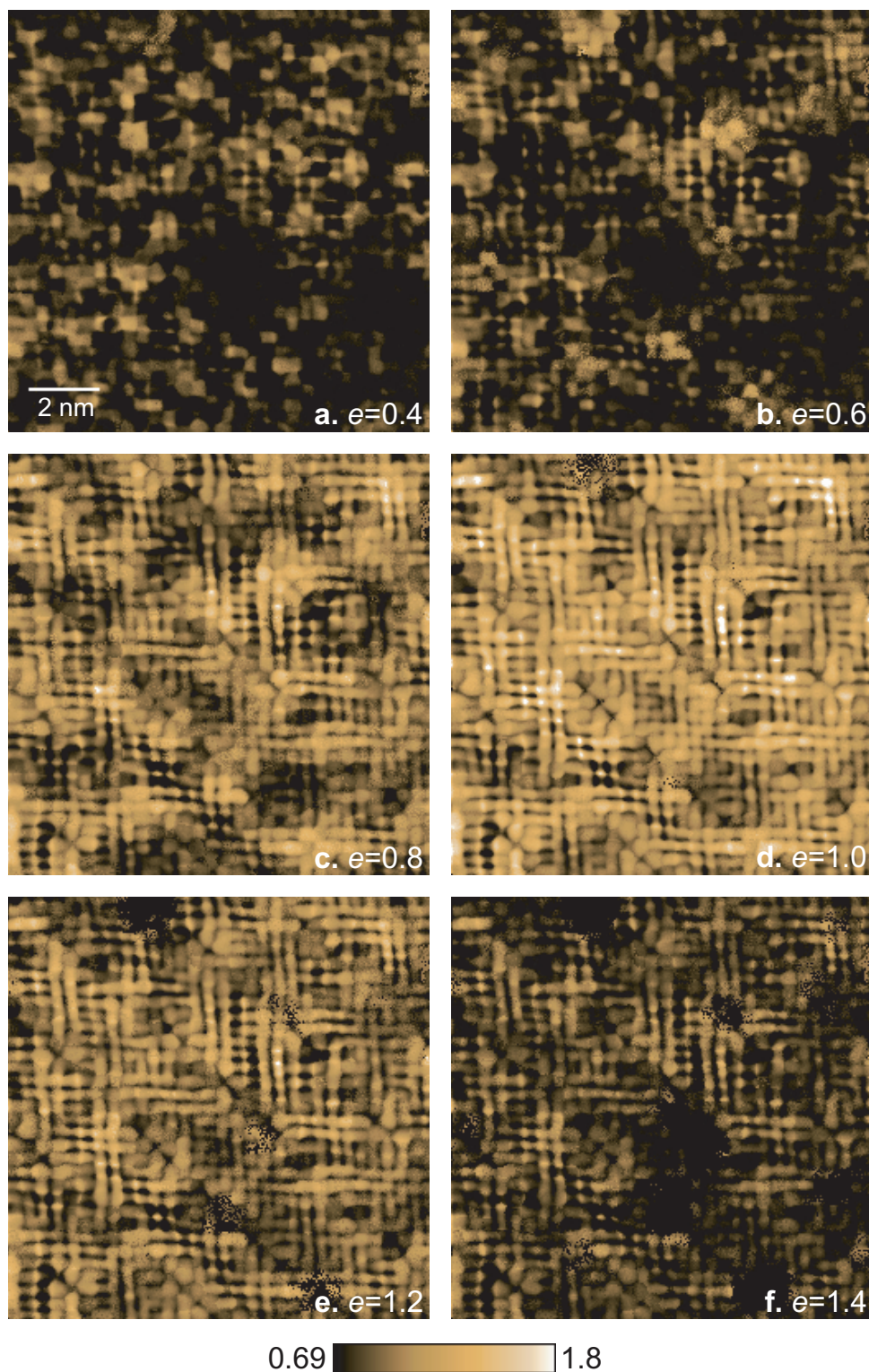


Figure 7. A series of images displaying the real space conductance ratio $Z(\mathbf{r}, e)$ as a function of energy rescaled to the local PG value, $e = E/\Delta_1(\mathbf{r})$. Each pixel location was rescaled independently of the others. The common color scale for all panels illustrates that the broken electronic symmetry patterns appear strongest in Z exactly at $E = \Delta_1(\mathbf{r})$, the local PG energy.

topographic image $T(\mathbf{r})$ perfectly a_0 -periodic; the same transformation is then applied to the simultaneously acquired $Z(\mathbf{r}, e)$ to register all the electronic structure data to this ideal lattice. The topograph $T(\mathbf{r})$ is shown in figure 8(a); the inset compares the Bragg peaks of its real (in-phase) Fourier components $\text{Re } T(Q_x)$, $\text{Re } T(Q_y)$ and demonstrates that $\text{Re } T(Q_x)/\text{Re } T(Q_y) = 1$. Therefore, $T(\mathbf{r})$ preserves the C_4 symmetry of the crystal lattice. In contrast, figure 8(b) shows that the $Z(\mathbf{r}, e = 1)$ determined simultaneously with figure 8(a) breaks various crystal symmetries [57–59]. The inset shows that since $\text{Re } Z(Q_x, e = 1)/\text{Re } Z(Q_y, e = 1) \neq 1$, the PG states break C_4 symmetry on average throughout figure 8(b). We defined a normalized measure of intra-unit cell nematic (C_2) symmetry over the entire FOV as a function of e ,

$$O_N^Q(e) \equiv \frac{\text{Re } Z(Q_y, e) - \text{Re } Z(Q_x, e)}{\bar{Z}(e)}, \quad (7)$$

where $\bar{Z}(e)$ is the spatial average of $Z(\mathbf{r}, e)$. The plot of $O_N^Q(e)$ in figure 8(c) shows that the magnitude of $O_N^Q(e)$ is low for $e \ll \Delta_0/\Delta_1$, begins to grow near $e \sim \Delta_0/\Delta_1$, and becomes well defined as $e \sim 1$ or $E \sim \Delta_1$. Thus, the observed intra-unit-cell C_4 symmetry breaking is specific to the PG states.

To explore the source of these effects within the CuO_2 unit cell, we study $Z(\mathbf{r}, e)$ with sub-unit-cell resolution. Figure 8(d) shows the topographic image of a representative region from figure 8(a); the locations of each Cu site \mathbf{R} , and of the two O atoms within its unit cell, are indicated. Figure 8(e) shows $Z(\mathbf{r}, e)$ measured simultaneously with figure 8(d) with the same Cu and O site labels. Next we define

$$O_N^R(e) = \sum_{\mathbf{R}} \frac{Z_x(\mathbf{R}, e) - Z_y(\mathbf{R}, e)}{\bar{Z}(e)N}, \quad (8)$$

where $Z_x(\mathbf{R}, e)$ is the magnitude of $Z(\mathbf{r}, e)$ at the O site $a_0/2$ along the x -axis from \mathbf{R} , while $Z_y(\mathbf{R}, e)$ is the equivalent along the y -axis, and N is the number of unit cells. This is the \mathbf{r} -space measure of C_2 symmetry that is equivalent to $O_N^Q(e)$ in equation (7) but counting only O site contributions. Figure 8(f) contains the calculated value of $O_N^R(e)$ from the same FOV as figures 8(a) and (b), revealing the good agreement with $O_N^Q(e)$.

7.4. Separating $E \sim \Delta_1$ broken electronic symmetry at intra-unit-cell from that at $\mathbf{Q} = \mathbf{S}_x, \mathbf{S}_y$

The smectic contributions to the $E \sim \Delta_1$ electronic structure can be examined by defining a measure analogous to equation (7) of C_4 symmetry breaking, but now in the modulations with $\mathbf{S}_x, \mathbf{S}_y$,

$$O_S^Q(e) = \frac{\text{Re } Z(S_y, e) - \text{Re } Z(S_x, e)}{\bar{Z}(e)}. \quad (9)$$

For all samples studied, the low values found for $|O_S^Q(e)|$ at low e occur because these states are dispersive Bogoliubov quasiparticles [59], [53–56] and cannot be analyzed in term of any static electronic structure, smectic or otherwise. More importantly, $|O_S^Q(e)|$ shows no tendency to become well established at the PG or any other energy [68].

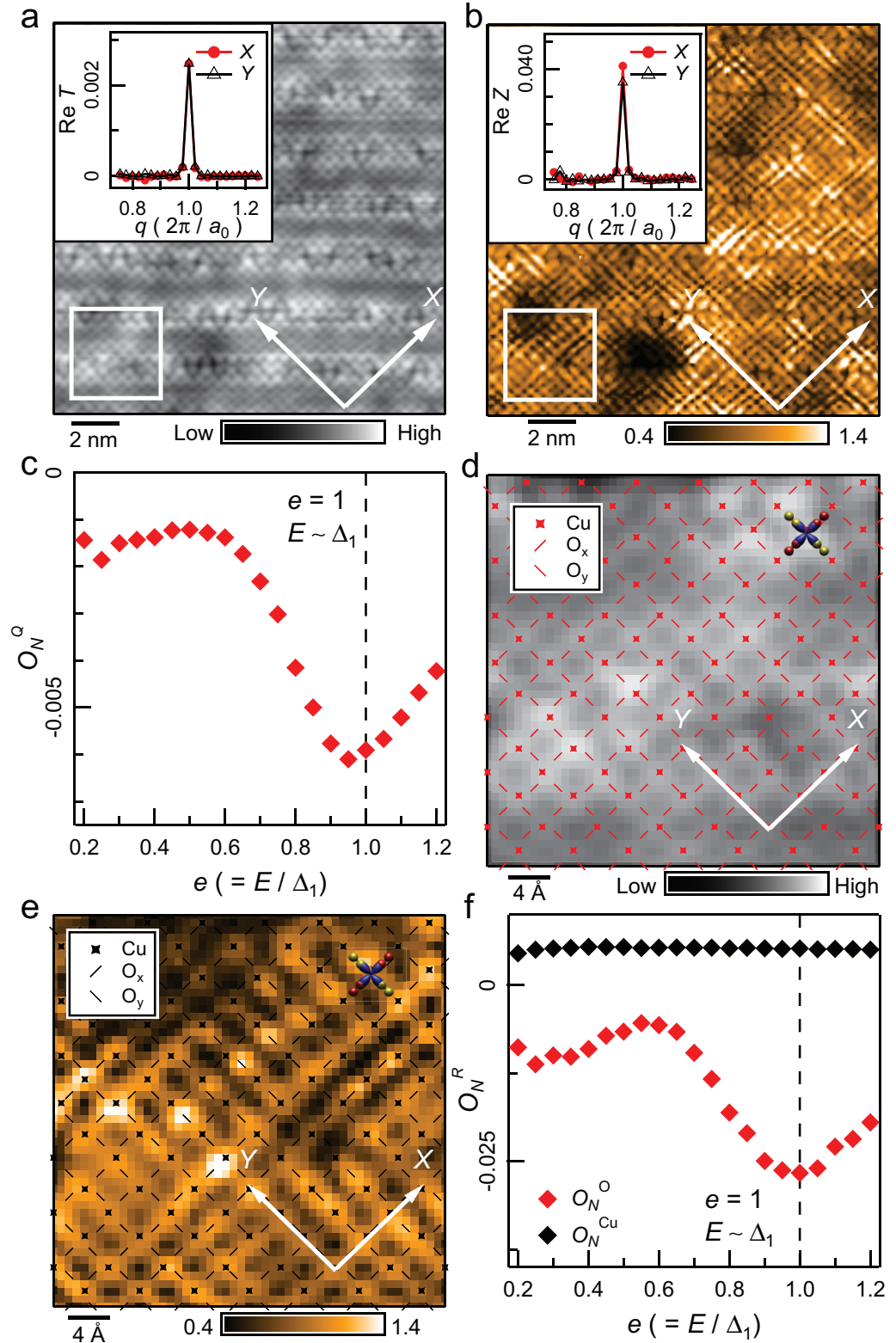


Figure 8. (a) Topographic image $T(\mathbf{r})$ of the $\text{Bi}_2\text{Sr}_2\text{CaCu}_2\text{O}_{8+\delta}$ surface. The inset shows that the real part of its Fourier transform $\text{Re } T(\mathbf{q})$ does not break C_4 symmetry at its Bragg points because plots of $T(\mathbf{q})$ show its values to be

Figure 8. (Continued) indistinguishable at $\mathbf{Q}_x = (1, 0)2\pi/a_0$ and $\mathbf{Q}_y = (0, 1)2\pi/a_0$. Importantly, this means that neither the crystal nor the tip used to image it (and its $Z(\mathbf{r}, E)$ simultaneously) breaks C_4 symmetry. (b) The $Z(\mathbf{r}, e=1)$ image measured simultaneously with $T(\mathbf{r})$ in (a). The inset shows that the Fourier transform $Z(\mathbf{q}, e=1)$ does break C_4 symmetry at its Bragg points because $\text{Re } Z(\mathbf{Q}_x, e \sim 1) \neq \text{Re } Z(\mathbf{Q}_y, e \sim 1)$. This means that, on average throughout the FOV of (a) and (b), the modulations of $Z(\mathbf{r}, E < \Delta_1)$ that are periodic with the lattice have different intensities along the x -axis and along the y -axis. (c) The value of $O_N^Q(e)$ defined in equation (7) computed from $Z(\mathbf{r}, e)$ data measured in the same FOV as (a) and (b). Its magnitude is low for all $E < \Delta_0$ and then rises rapidly to become well established near $e < 1$ or $E < \Delta_1$. Thus, the quantitative measure of intra-unit-cell electronic nematicity reveals that the PG states in this FOV of a strongly underdoped $\text{Bi}_2\text{Sr}_2\text{CaCu}_2\text{O}_{8+\delta}$ sample break the expected C_4 symmetry of the CuO_2 electronic structure. (d) Topographic image $T(\mathbf{r})$ from the region identified by a small white box in (a). It is labeled with the locations of the Cu atom plus both O atoms within each CuO_2 unit cell (labels shown in the inset). (e) The simultaneous $Z(\mathbf{r}, e=1)$ image in the same FOV as (d) (the region identified by small white box in (b)) showing the same Cu and O site labels within each unit cell (see inset). Thus, the physical locations at which the nematic measure $O_N^R(e)$ of equation (8) is evaluated are labeled by the dashes. (f) The value of $O_N^R(e)$ computed from $Z(\mathbf{r}, e)$ data measured in the same FOV as (a) and (b). As in (c), its magnitude is low for all $E < \Delta_0$ and then rises rapidly to become well established at $e \sim 1$ or $E \sim \Delta_1$.

To visualize the separate broken symmetries in the $E \sim \Delta_1$ electronic structure, we consider $Z(\mathbf{q}, e=1)$ in figure 9(a); this is the Fourier-space representation of electronic structure of the $E \sim \Delta_1$ states. Taking into account only the Bragg peaks at $\mathbf{Q}_x, \mathbf{Q}_y$ (red circles/arrows in figure 9(a)), the C_4 symmetry breaking of $\mathbf{Q} = 0$ intra-unit-cell electronic structure is revealed, as shown schematically in figure 9(b). By contrast, if one focuses upon the incommensurate modulations $\mathbf{S}_x, \mathbf{S}_y$ (blue circles/arrows in figure 9(a)), one finds a disordered electronic structure with incommensurate modulations that break both C_2 and translational symmetry locally, as shown schematically in figure 9(c). Although these two types of electronic phenomena represent clearly distinct broken symmetries, SI-STM reveals that they coexist in the $E \sim \Delta_1$ PG electronic structure of underdoped cuprates [68].

7.5. Summary

When $Z(\mathbf{r}, E)$ images of the intra-unit-cell electronic structure in underdoped $\text{Bi}_2\text{Sr}_2\text{CaCu}_2\text{O}_{8+\delta}$ are analyzed using two independent techniques, compelling evidence for intra-unit-cell (or $\mathbf{Q} = 0$) electronic symmetry breaking is detected specifically of the states at the $E \sim \Delta_1$ PG energy. Moreover, this intra-unit-cell symmetry breaking coexists with finite $\mathbf{Q} = \mathbf{S}_x, \mathbf{S}_y$ smectic electronic modulations, but they can be analyzed separately by using Fourier filtration techniques. The wavevector of smectic electronic modulations is controlled by the point in \mathbf{k} -space where the Bogoliubov interference signature disappears when the arc supporting

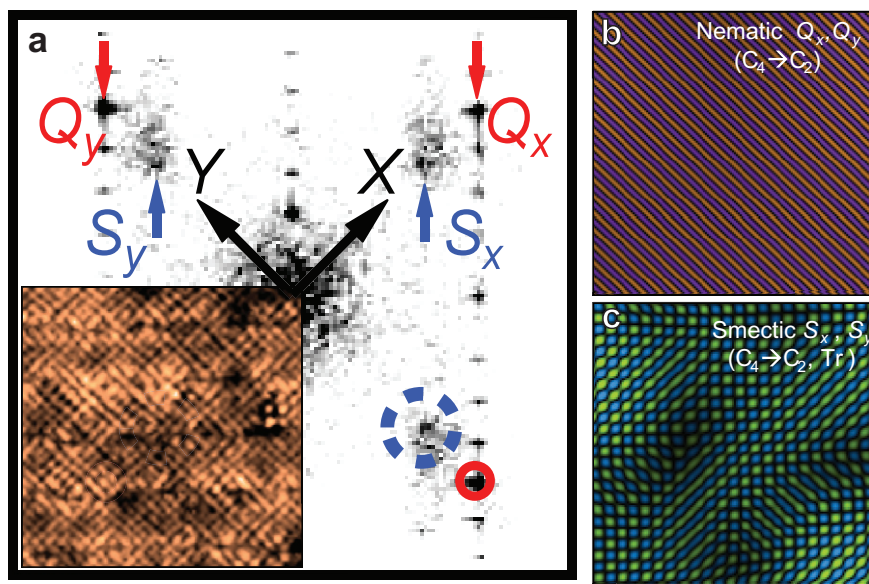


Figure 9. (a) The Fourier transform $Z(\mathbf{q}, e = 1)$ of a typical image $Z(\mathbf{r}, e = 1)$ of the spatial structure of the PG states in underdoped $\text{Bi}_2\text{Sr}_2\text{CaCu}_2\text{O}_{8+\delta}$. The Bragg peaks are identified by red circles and $\mathbf{Q}_x, \mathbf{Q}_y$ labels. The wavevectors of the smectic modulations in electron structure are identified by blue circles and $\mathbf{S}_x, \mathbf{S}_y$ labels. (b) Schematic depiction of how the spatial information in the inequivalent Bragg peaks $\mathbf{Q}_x, \mathbf{Q}_y$ alone could reveal intra unit-cell C_2 -symmetric electronic structure. (c) Schematic depiction of how the spatial information in the $\mathbf{S}_x, \mathbf{S}_y$ wavevectors alone can reveal the disordered breaking of both rotational and translational symmetry in electronic structure.

delocalized Cooper-pairing approaches the lines between $\mathbf{k} = \pm(0, \pi/a_0)$ and $\mathbf{k} = \pm(\pi/a_0, 0)$ (see figures 5(b)–(d)). This appears to indicate that the $\mathbf{Q} = \mathbf{S}_x, \mathbf{S}_y$ smectic effects are dominated by the same \mathbf{k} -space phenomena that restrict the regions of Cooper pairing [58].

8. Overview, conclusions and future

8.1. Bipartite electronic structure of underdoped cuprates derived from SI-STM

A clearer picture of the fundamentally bipartite structure of electronic excitations in strongly underdoped cuprates approaching the Mott insulator emerges from these SI-STM studies. This is summarized in figure 10. In the dSC phase (figures 10(a)–(c)), the Bogoliubov QPI signature of delocalized Cooper pairs (section 5 and figure 10(c)) exists upon the arc in \mathbf{k} -space labeled by region II in figure 10(a). The Bogoliubov QPI disappears near the lines connecting $\mathbf{k} = (0, \pm\pi/a_0)$ to $\mathbf{k} = (\pm\pi/a_0, 0)$ —thus defining a \mathbf{k} -space arc that supports the delocalized Cooper pairing. This arc shrinks rapidly towards the $\mathbf{k} = (\pm\pi/2a_0, \pm\pi/2a_0)$ points with falling hole density in a fashion, which could satisfy Luttinger’s theorem if it were actually a hole-pocket bounded from behind by the $\mathbf{k} = \pm(\pi/a_0, 0)$ – $\mathbf{k} = \pm(0, \pi/a_0)$ lines. The $E \sim \Delta_1$ PG excitations (section 7) are labeled by region I in figure 10(a) and exhibit a radically different \mathbf{r} -space phenomenology, locally breaking the expected C_4 symmetry of electronic structure

at least down to C_2 and possibly to an even lower symmetry, within each CuO_2 unit cell (figure 10(b)). These intra-unit-cell broken electronic symmetry states coexist with finite $\mathbf{Q} = \mathbf{S}_x, \mathbf{S}_y$ modulations that break translational and rotational symmetry very locally. In the PG phase (figures 10(d)–(f)), the Bogoliubov QPI signature (section 6 and figure 10(f)) exists upon a smaller part of the same arc in \mathbf{k} -space as it did in the dSC phase. This is labeled as region II in figure 10(d). Here, however, since the ungapped Fermi arc (region III) predominates, the gapped region supporting d-wave QPI has shrunk into a narrow sliver near a line connecting $\mathbf{k} = (\pi/a_0, 0)$ and $\mathbf{k} = (0, \pi/a_0)$ (figure 10(d)). The $E \sim \Delta_1$ excitations in the PG phase (section 7) are again labeled by region I in figure 10(d), and exhibit $\mathbf{Q} = 0$ and $\mathbf{Q} = \mathbf{S}_x, \mathbf{S}_y$ broken electronic symmetries indistinguishable from those in the dSC phase (figure 10(e)).

8.2. Microscopic mechanism of intra-unit-cell electronic symmetry breaking

The microscopic source of the intra-unit-cell electronic symmetry breaking in the $E \sim \Delta_1$ states (figure 8) is unknown at present. One important point to consider is the relationship between ARPES, elastic neutron scattering (NS) and SI-STM studies of broken electronic symmetries of the PG phase. ARPES reveals spontaneous dichroism of antinodal states [100], which break C_4 symmetry because the opposite sign of the effect occurs at $\mathbf{k} = (\pi/a_0, 0)$ and $\mathbf{k} = (0, \pi/a_0)$. The intra-unit-cell magnetic order detected by NS at the Bragg peak [101, 102] consists of apparently antiferromagnetic and C_4 -breaking states in both $\text{YBa}_2\text{Cu}_3\text{O}_{6+x}$ and $\text{HgBa}_2\text{CuO}_{4+\delta}$. The SI-STM studies also reveal intra-unit cell, C_4 -breaking states at the PG energy (section 7). With such commonality between the results from such disparate techniques, it is not implausible that they are detecting different characteristics of the same broken symmetry states. If so, an immediate consequence of the existence of the intra-unit-cell electronic/magnetic structures within the CuO_2 unit cell would be that an effective model defined purely on the copper lattice (such as the t - J -type of model) will be unable to capture the physics of underdoped cuprates.

8.3. Relationship between the two broken electronic symmetries and the superconductivity

Both nematic and smectic broken symmetries have been reported in the electronic structure of different cuprate compounds [103–106]. A spin/charge smectic broken symmetry phase (stripes) exists in $\text{La}_{2-x-y}\text{Nd}_y\text{Sr}_x\text{CuO}_4$ and $\text{La}_{2-x}\text{Ba}_x\text{CuO}_4$ when $p \sim 0.125$. Nematic broken symmetry has been reported in underdoped $\text{YBa}_2\text{Cu}_3\text{O}_{6+\delta}$ [101], underdoped $\text{Bi}_2\text{Sr}_2\text{CaCu}_2\text{O}_{8+\delta}$ [68, 100] and underdoped $\text{HgBa}_2\text{CuO}_{4+x}$ [102]. To understand how both of these distinct broken symmetry states can coexist, and to determine the form of their interactions, will be important in unraveling the mystery of the cuprate phase diagram. That equivalent broken symmetries appear to coexist at the nanoscale in the electronic structure of $\text{Bi}_2\text{Sr}_2\text{CaCu}_2\text{O}_{8+\delta}$ ([68] and figure 9) represents an important new opportunity to understand their interactions. Should that be possible, the next challenge for SI-STM would be to demonstrate directly the relationship between the superconductivity and the broken symmetries of the $E \sim \Delta_1$ PG states with the (ambitious) view towards a complete Ginzburg–Landau understanding of the cuprate phase diagram.

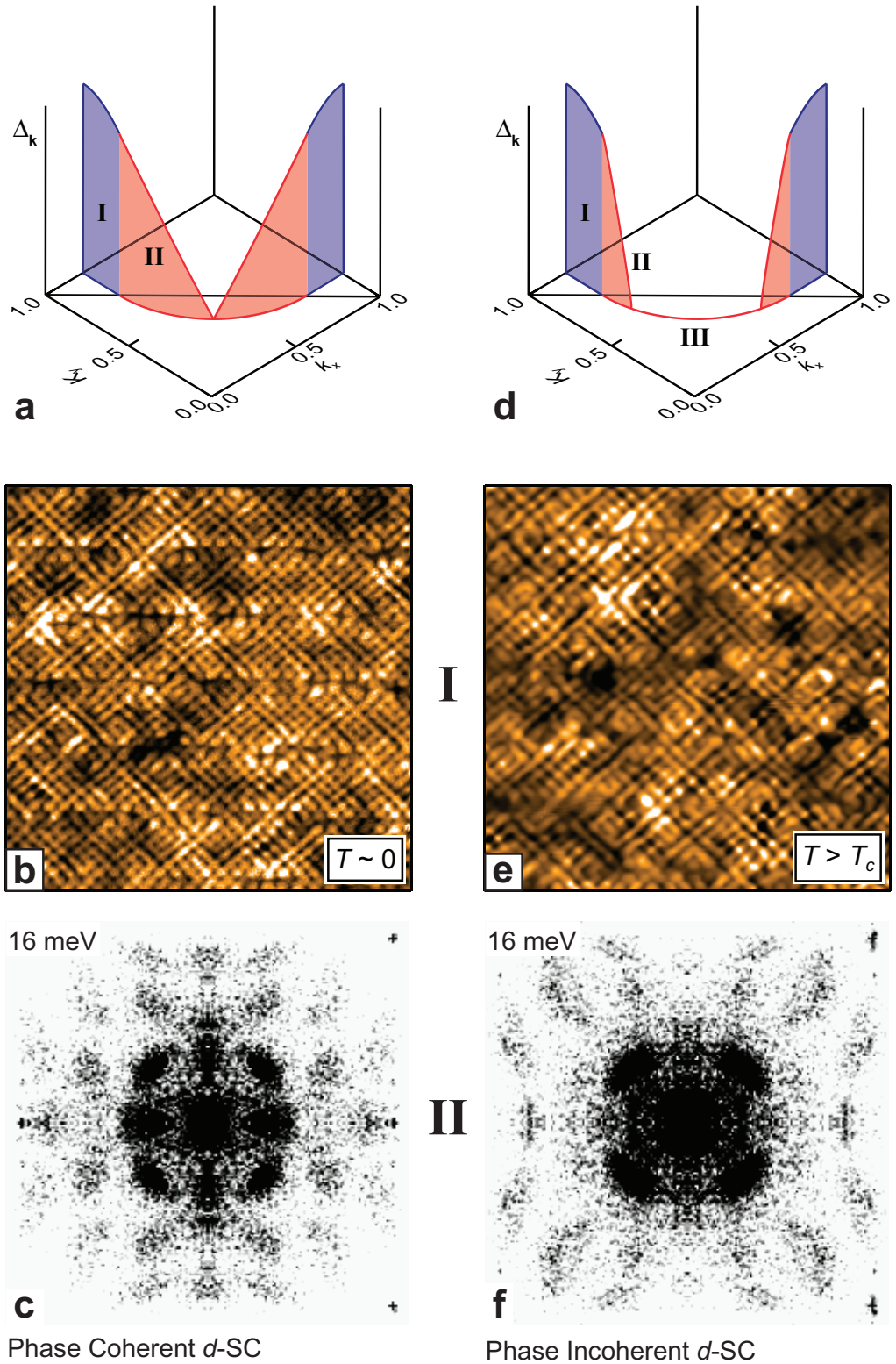


Figure 10. (a) A schematic representation of the electronic structure in one quarter of the Brillouin zone at the lowest temperatures in the dSC phase. The region marked II in front of the line joining $\mathbf{k} = (\pi/a_0, 0)$ and $\mathbf{k} = (0, \pi/a_0)$ is the locus of the Bogoliubov QPI signature of delocalized Cooper pairs.

Figure 10. (Continued) (b) An example of the broken spatial symmetries that are concentrated on the PG energy $E \sim \Delta_1$ as measured at lowest temperatures. (c) An example of the characteristic Bogoliubov QPI signature of 16 pairs of interference wavevectors, all dispersive and internally consistent with the octet model as well as particle-hole symmetric $\mathbf{q}_i(+E) = \mathbf{q}_i(-E)$, here measured at the lowest temperatures. (d) A schematic representation of the electronic structure in one quarter of the Brillouin zone at $T \sim 1.5T_c$ in the PG phase. The region marked III is the Fermi arc, which is seen in QPI studies as a set of interference wavevectors $\mathbf{q}_i(E = 0)$, which indicate that there is no gap node at $E = 0$. Region II in front of the line joining $\mathbf{k} = (\pi/a_0, 0)$ and $\mathbf{k} = (0, \pi/a_0)$ is the locus of the phase incoherent Bogoliubov QPI signature. Here, all 16 pairs of wavevectors of the octet model are detected and found to be dispersive. Thus, although the sample is not a long-range phase-coherent superconductor, it does give clear QPI signatures of d-wave Cooper pairing. (e) An example of the broken spatial symmetries that are concentrated on PG energy $E \sim \Delta_1$ as measured in the PG phase; they are indistinguishable from measurements at $T \sim 0$. (f) An example of the characteristic Bogoliubov QPI signature of sixteen pairs of interference wavevectors, all dispersive and internally consistent with the octet model as well as particle-hole symmetric $\mathbf{q}_i(+E) = \mathbf{q}_i(-E)$, here measured at $T \sim 1.5T_c$.

8.4. Electronic structure of the cuprate PG phase

Among the explanations for the PG phase is that it is a spin liquid created by hole-doping an antiferromagnetic Mott insulator, or that it is a d-wave superconductor without phase coherence, or that it is an electronic ordered phase with additional broken symmetries. SI-STM reveals that the basic particle-hole symmetric, dispersive, octet phenomenology is consistent with theoretical predictions for the QPI characteristics of a phase incoherent d-wave superconductor (figure 10(f)). Further, since all the $\mathbf{q}_i(E)$ $i = 1, \dots, 7$ disperse internally consistently with the octet model, they cannot represent the signature of any static ordered state of fixed wavevector \mathbf{Q}^* . Thus, the low-energy $E < \Delta_0$ electronic structure of the PG phase (which is what is probed by transport and thermodynamics) is indeed consistent with expectations for a phase-incoherent d-wave superconductor. Nevertheless, the high-energy electronic states at the PG energy scale $E \sim \Delta_1$ exhibit strongly broken symmetries, including intra-unit-cell symmetry breaking and finite \mathbf{Q} smectic modulations (figure 9). Finally, the truncated arc of Bogoliubov QPI seen below T_c , which remains unchanged in the PG phase except for the appearance of an ungapped portion, appears not-inconsistent with the phenomenological models proposed for a spin liquid (see below). Thus, the characteristics of the PG phase determined by SI-STM contain some elements of all three theoretical approaches to the electronic structure of hole-doped CuO_2 approaching the Mott insulator.

8.5. Fundamental electronic structure of the hole-doped CuO_2 Mott insulator from SI-STM

The overall electronic structure of underdoped cuprates as derived from SI-STM studies (figure 10) motivates a number of questions. Why does the Bogoliubov QPI signature of delocalized Cooper pairs disappear [58] near the $\mathbf{k} = (0, \pm\pi/a_0)$ – $\mathbf{k} = (\pm\pi/a_0, 0)$ connecting

lines? And why do the PG states $E \sim \Delta_1$ exhibit such dramatically different symmetries [57, 68] to the coexisting Bogoliubov quasiparticles at $E < \Delta_0$? One reason could be that the \mathbf{r} -space electronic structure has undergone a $\sqrt{2} \times \sqrt{2}$ reconstruction due to the appearance of a coexisting long-range ordered state. The arcs supporting Cooper pairing would then represent one side of a hole-pocket within a reduced Brillouin zone. But neither antiferromagnetism nor other long-range ordered electronic phases [23, 24] necessary for such a reconstruction have yet been detected in $\text{Bi}_2\text{Sr}_2\text{CaCu}_2\text{O}_{8+\delta}$. A related explanation could be inelastic scattering of the quasiparticles by spin fluctuations [107, 108] at $\mathbf{Q} = (\pi/a_0, \pi/a_0)$ or by fluctuations of other ordered states that would exhibit a $\sqrt{2} \times \sqrt{2}$ reconstruction if stabilized. Neither of these approaches explains the broken spatial symmetries of the $E \sim \Delta_1$ PG states, however. Another type of explanation could be a spin-charge stripe glass [57] coexisting with superconductivity [109–112]. This could explain the loss of translational symmetry and the C_4 breaking within the $E \sim \Delta_1$ PG states, and perhaps the disappearance of quasiparticle interference along the $\mathbf{k} = (0, \pm\pi/a_0)$ – $\mathbf{k} = (\pm\pi/a_0, 0)$ lines [90, 113], but it does not (yet) explain the intra-unit-cell C_4 -breaking in electronic symmetry. Yet another proposal, that orbital charge currents exist within each CuO_2 unit cell [22], receives support from NS experiments [101, 102] and may provide an explanation for the intra-unit-cell electronic symmetry breaking discussed here (although reasons why such an orbiting current could be detected by SI-STM are unknown). But it does not (yet) explain the finite \mathbf{Q} smectic modulations or the disappearance of Bogoliubov QPI near $\mathbf{k} = (0, \pm\pi/a_0)$ – $\mathbf{k} = (\pm\pi/a_0, 0)$ lines. A final possibility, which is revealed by the fact that the Luttinger theorem can be satisfied by using the region bounded the Bogoliubov QPI arcs and the $\mathbf{k} = (0, \pm\pi/a_0)$ – $\mathbf{k} = (\pm\pi/a_0, 0)$ lines [58], is that many of the effects summarized in figure 10 are properties of a hole-doped spin liquid [15]. This approach might explain (at least phenomenologically) the Bogoliubov arc termination as where the Green's-function poles turn to zeros along the $\mathbf{k} = (0, \pm\pi/a_0)$ – $\mathbf{k} = (\pm\pi/a_0, 0)$ lines [15, 58], how the Luttinger theorem can be satisfied given the exotic \mathbf{k} -space structure observed [15, 58], and possibly the cause of smectic finite- \mathbf{Q} non-dispersive modulations [114]. However, it does not (yet) appear to explain the intra-unit-cell electronic symmetry breaking.

When the electronic structure of underdoped cuprates is examined with high resolution both in \mathbf{r} -space and \mathbf{k} -space using SI-STM, a highly complex phenomenology is revealed. As is often the case, if one focuses on a single element within such a ramified phenomenology, there are several theoretical models available to explain it. One hopes, however, that the eventual overarching theory of cuprate high-temperature superconductivity will explain the complete phenomenology in a unified fashion—as the Bardeen–Cooper–Schrieffer theory did for conventional superconductors. In this review, we attempt to contribute to such an aspiration by summarizing what we think are the most important elements of cuprate electronic structure phenomenology revealed by a decade of SI-STM studies. The key questions emerging from this effort are whether the observed broken symmetries (and/or perhaps others yet to be discovered) are responsible for the opening of the PG and, if so, how these exotic broken symmetry states interact with the superconducting components of the CuO_2 electronic structure.

Acknowledgments

We acknowledge and thank all of our collaborators: J W Alldredge, I Firmo, M H Hamidian, T Hanaguri, P J Hirschfeld, J E Hoffman, E W Hudson, Chung Koo Kim, Y Kohsaka, K M Lang, C Lupien, Jinhwan Lee, Jinho Lee, V Madhavan, K McElroy, J Orenstein, S H Pan,

R Simmonds, J Slezak, J Sethna, H Takagi, C Taylor, P Wahl and M Wang. Preparation of this review was supported by the Center for Emergent Superconductivity, an Energy Frontier Research Center funded by the US Department of Energy, Office of Basic Energy Sciences under Award number DE-2009-BNL-PM015.

References

- [1] Zaanen J, Sawatzky G A and Allen J W 1985 Band gaps and electronic structure of transition-metal compounds *Phys. Rev. Lett.* **55** 418
- [2] Anderson P W 1950 Antiferromagnetism. Theory of superexchange interaction *Phys. Rev.* **79** 350
- [3] Anderson P W 1987 The resonating valence bond state in La_2CuO_4 *Science* **6** 1196
- [4] Chen C T *et al* 1991 Electronic states in $\text{La}_{2-x}\text{Sr}_x\text{CuO}_{4-\delta}$ probed by soft-x-ray Absorption *Phys. Rev. Lett.* **66** 104
- [5] Orenstein J and Millis A J 2000 Advances in the physics of high-temperature superconductivity *Science* **288** 468
- [6] Timusk T and Statt B 1999 The pseudogap in high-temperature superconductors: an experimental survey *Rep. Prog. Phys.* **62** 61
- [7] Hüfner S, Hossain M A, Damascelli A and Sawatzky G A 2008 Two gaps make a high-temperature superconductor? *Rep. Prog. Phys.* **71** 062501
- [8] Damascelli A, Hussain Z and Shen Z-X 2003 Angle-resolved photoemission studies of the cuprate superconductors *Rev. Mod. Phys.* **75** 473
- [9] Campuzano J C, Norman M R and Randeria M 2004 *The Physics of Superconductors* vol II ed K H Bennemann and J B Ketterson (New York: Springer) pp 167–273
- [10] Norman M R and Papin C 2003 The electronic nature of high temperature cuprate superconductors *Rep. Prog. Phys.* **66** 1547
- [11] Zhang F C, Gros C, Rice T M and Shiba H 1988 A renormalized Hamiltonian approach to a resonant valence bond wavefunction *Supercond. Sci. Technol.* **1** 36–46
- [12] Kotliar G 1988 Resonating valence bonds and d -wave superconductivity *Phys. Rev. B* **37** 3664–6
- [13] Paramakanti A, Randeria M and Trivedi N 2001 Projected wave functions and high temperature superconductivity *Phys. Rev. Lett.* **87** 217002
- [14] Anderson P W, Lee P A, Randeria M, Rice T M, Trivedi N and Zhang F C 2004 The physics behind high-temperature superconducting cuprates: the ‘plain vanilla’ version of RVB *J. Phys.: Condens. Matter* **16** R755–69
- [15] Yang K Y, Rice T M and Zhang F C 2006 Phenomenological theory of the pseudogap state *Phys. Rev. B* **73** 174501
- [16] Randeria M, Trivedi N, Moreo A and Scalettar R T 1992 Pairing and spin gap in the normal state of short coherence length superconductors *Phys. Rev. Lett.* **69** 2001–4
- [17] Emery V J and Kivelson S A 1995 Importance of phase fluctuations in superconductors with small superfluid density *Nature* **374** 434–7
- [18] Franz M and Millis A J 1998 Phase fluctuations and spectral properties of underdoped cuprates *Phys. Rev. B* **58** 14572–80
- [19] Carlson E W, Kivelson S A, Emery V J and Manousakis E 1999 Classical phase fluctuations in high temperature superconductors *Phys. Rev. Lett.* **83** 612–5
- [20] Kwon H-J, Dorsey A T and Hirschfeld P J 2001 Observability of quantum fluctuations in cuprate superconductors *Phys. Rev. Lett.* **86** 3875–8
- [21] Berg E and Altman E 2007 Evolution of the Fermi surface of d -wave superconductors in the presence of thermal phase fluctuations *Phys. Rev. Lett.* **99** 247001
- [22] Varma C M 2006 Theory of the pseudogap state of the cuprates *Phys. Rev. B* **73** 155113

- [23] Lee P A, Nagaosa N and Wen X-G 2006 Doping a mott insulator: physics of high-temperature superconductivity *Rev. Mod. Phys.* **78** 17–85
- [24] Chakravarty S, Laughlin R B, Morr D K and Nayak C 2001 Hidden order in the cuprates *Phys. Rev. B* **63** 094503
- [25] Honerkamp C, Fu H C and Lee D-H 2007 Phonons and d-wave pairing in the two-dimensional Hubbard model *Phys. Rev. B* **75** 014503
- [26] Newns D M and Tsuei C C 2007 Fluctuating Cu-O-Cu bond model of high-temperature superconductivity *Nat. Phys.* **3** 184–91
- [27] Zaanen J and Gunnarsson O 1989 Charged magnetic domain lines and the magnetism of high- T_c oxides *Phys. Rev. B* **40** 7391–4
- [28] Emery V J, Kivelson S A and Tranquada J M 1999 Stripe phases in high-temperature superconductors *Proc. Natl Acad. Sci. USA* **96** 8814–7
- [29] White S R and Scalapino D J 1998 Density matrix renormalization group study of the striped phase in the 2D t - J model *Phys. Rev. Lett.* **80** 1272–5
- [30] Kivelson S A, Fradkin E and Emery V J 1998 Electronic liquid-crystal phases of a doped Mott insulator *Nature* **393** 550–3
- [31] Vojta M and Sachdev S 1999 Charge order, superconductivity, and a global phase diagram of doped antiferromagnets *Phys. Rev. Lett.* **83** 3916–9
- [32] Kivelson S A *et al* 2003 How to detect fluctuating stripes in the high-temperature superconductors *Rev. Mod. Phys.* **75** 1201–41
- [33] Sachdev S 2003 Colloquium: Order and quantum phase transitions in the cuprate superconductors *Rev. Mod. Phys.* **75** 913–2
- [34] Vojta M 2009 Lattice symmetry breaking in cuprate superconductors: stripes, nematics, and superconductivity *Adv. Phys.* **58** 699–820
- [35] Kim E-A, Lawler M J, Oretto P, Sachdev S, Fradkin E and Kivelson S A 2008 Theory of the nodal nematic quantum phase transition in superconductors *Phys. Rev. B* **77** 184514
- [36] Fradkin E, Kivelson S A, Lawler M J, Eisenstein J P and Mackenzie A P 2010 Nematic Fermi fluids in condensed matter physics *Annu. Rev. Condens. Matter Phys.* **1** 153–78
- [37] Gedik N, Orenstein J, Liang R, Bonn D A and Hardy W N 2003 Diffusion of Nonequilibrium quasi-particles in a cuprate superconductor *Science* **300** 1410–2
- [38] Deutscher G 1999 Coherence and single-particle excitations in the high-temperature superconductors *Nature* **397** 410–2
- [39] Tacon M L *et al* 2006 Two energy scales and two distinct quasiparticle dynamics in the superconducting state of underdoped cuprates *Nat. Phys.* **2** 537–43
- [40] Khasanov R *et al* 2010 Suppression of the antinodal coherence of $(\text{Bi, Pb})_2(\text{Sr, La})_2\text{CuO}_{6+\delta}$ as revealed by muon spin rotation and angle-resolved photoemission *Phys. Rev. B* **82** 020511(R)
- [41] Norman M R *et al* 1998 Destruction of the Fermi surface in underdoped high- T_c superconductors *Nature* **392** 157–60
- [42] Shen K M *et al* 2005 Nodal quasiparticles and antinodal charge ordering in $\text{Ca}_{2-x}\text{Na}_x\text{CuO}_2\text{Cl}_2$ *Science* **307** 901–4
- [43] Tanaka K *et al* 2006 Distinct Fermi-momentum-dependent energy gaps in deeply underdoped Bi2212 *Science* **314** 1910–3
- [44] Kanigel A *et al* 2006 Evolution of the pseudogap from Fermi arcs to the nodal liquid *Nat. Phys.* **2** 447–51
- [45] Kanigel A *et al* 2007 Protected nodes and the collapse of Fermi arcs in high- T_c cuprate superconductors *Phys. Rev. Lett.* **99** 157001
- [46] Kondo T, Khasanov R, Takeuchi T, Schmalian J and Kaminski A 2009 Competition between the pseudogap and superconductivity in the high- T_c copper oxides *Nature* **457** 296–300
- [47] Yang H-B, Ramaeu J D, Pan Z-H, Gu G D, Johnson P D, Claus R H, Hinks D G and Kidd T E 2010 On the reconstructed Fermi surface in the underdoped cuprates arXiv:1008.3121

- [48] Renner C, Revaz B, Genoud J-Y, Kadowaki K and Fischer Ø 1998 Pseudogap precursor of the superconducting gap in under- and overdoped $\text{Bi}_2\text{Sr}_2\text{CaCu}_2\text{O}_{8+\delta}$ *Phys. Rev. Lett.* **80** 149–52
- [49] Fischer Ø, Kugler M, Maggio-Aprile I, Berthod C and Renner C 2007 Scanning tunneling spectroscopy of high-temperature superconductors *Rev. Mod. Phys.* **79** 353–419
- [50] McElroy K *et al* 2005 Coincidence of checkerboard charge order and antinodal state decoherence in strongly underdoped superconductor *Phys. Rev. Lett.* **94** 197005
- [51] McElroy K *et al* 2005 Atomic-scale sources and mechanism of the nanoscale electronic disorder in $\text{Bi}_2\text{Sr}_2\text{CaCu}_2\text{O}_{8+\delta}$ *Science* **309** 1048–52
- [52] Alldredge J W *et al* 2008 Evolution of the electronic excitation spectrum with strongly diminishing hole-density in superconducting $\text{Bi}_2\text{Sr}_2\text{CaCu}_2\text{O}_{8+\delta}$ *Nat. Phys.* **4** 319–26
- [53] Hoffman J E *et al* 2002 Imaging quasiparticle interference in $\text{Bi}_2\text{Sr}_2\text{CaCu}_2\text{O}_{8+\delta}$ *Science* **297** 1148–51
- [54] McElroy K *et al* 2003 Relating atomic-scale electronic phenomena to wave-like quasiparticle states in superconducting $\text{Bi}_2\text{Sr}_2\text{CaCu}_2\text{O}_{8+\delta}$ *Nature* **422** 592–6
- [55] Hanaguri T *et al* 2007 Quasiparticle interference and superconducting gap in $\text{Ca}_{2-x}\text{Na}_x\text{CuO}_2\text{Cl}_2$ *Nat. Phys.* **3** 865–71
- [56] Wise W D *et al* 2008 Charge-density-wave origin of cuprate checkerboard visualized by scanning tunnelling microscopy *Nat. Phys.* **4** 696–9
- [57] Kohsaka Y *et al* 2007 An intrinsic bond-centered electronic glass with unidirectional domains in underdoped cuprates *Science* **315** 1380–5
- [58] Kohsaka Y *et al* 2008 How cooper pairs vanish approaching the Mott insulator in $\text{Bi}_2\text{Sr}_2\text{CaCu}_2\text{O}_{8+\delta}$ *Nature* **454** 1072–8
- [59] Jhinhwan L *et al* 2009 Spectroscopic signature of phase incoherent superconductivity in underdoped $\text{Bi}_2\text{Sr}_2\text{CaCu}_2\text{O}_{8+\delta}$ *Science* **325** 1099–103
- [60] Pan S *et al* 2001 Microscopic electronic inhomogeneity in the high- T_c superconductor $\text{Bi}_2\text{Sr}_2\text{CaCu}_2\text{O}_{8+\delta}$ *Nature* **413** 282–5
- [61] Lang K M *et al* 2002 Imaging the granular structure of high- T_c superconductivity in underdoped $\text{Bi}_2\text{Sr}_2\text{CaCu}_2\text{O}_{8+\delta}$ *Nature* **415** 412–6
- [62] Cren T, Rditchev D, Sacks W and Lkein J 2001 Nanometer scale mapping of the density of states in an inhomogeneous superconductor *Euro. Phys. Lett.* **54** 84–90
- [63] Howald C, Fournier P and Kapitulnik A 2001 Inherent inhomogeneities in tunneling spectra of $\text{Bi}_2\text{Sr}_2\text{CaCu}_2\text{O}_{8-x}$ crystals *Phys. Rev. B* **64** 100504
- [64] Matsuda A, Fujii T and Watanabe T 2003 Gap inhomogeneity, phase separation and a pseudogap in $\text{Bi}_2\text{Sr}_2\text{CaCu}_2\text{O}_{8+\delta}$ *Physica C* **388** 207–8
- [65] Boyer M C *et al* 2007 Imaging the two gaps of the high-temperature superconductor $\text{Bi}_2\text{Sr}_2\text{CuO}_{6+x}$ *Nat. Phys.* **3** 802–6
- [66] Gomes K K, Pasupathy A N, Pushp A, Ono S, Ando Y and Yazdani A 2007 Visualizing pair formation on the atomic scale in the high- T_c superconductor $\text{Bi}_2\text{Sr}_2\text{CaCu}_2\text{O}_{8+\delta}$ *Nature* **447** 569–72
- [67] Pushp A *et al* 2009 Extending universal nodal excitations optimizes superconductivity in $\text{Bi}_2\text{Sr}_2\text{CaCu}_2\text{O}_{8+\delta}$ *Science* **324** 1689–93
- [68] Lawler M J *et al* 2010 Intra-unit-cell electronic nematicity of the High- T_c copper-oxide pseudogap states *Nature* **466** 374–51
- [69] Jenkins N *et al* 2009 Imaging the essential role of spin fluctuations in high- T_c superconductivity *Phys. Rev. Lett.* **103** 227001
- [70] Maekawa S *et al* 2004 *Physics of Transition Metal Oxides* (Berlin: Springer)
- [71] Eisaki H *et al* 2004 Effect of chemical inhomogeneity in bismuth-based copper oxide superconductors *Phys. Rev. B* **69** 064512
- [72] Wang Q-H, Han J H and Lee D-H 2002 Pairing near the Mott insulating limit *Phys. Rev. B* **65** 054501
- [73] Martin I and Balatsky A V 2001 Doping-induced inhomogeneity in high- T_c superconductors *Physica C* **357** 46–8

- [74] Zhu J-X, Ahn K H, Nussinov Z, Lookman T, Balatsky A V and Bishop A R 2003 Elasticity-driven nanoscale electronic structure in superconductors *Phys. Rev. Lett.* **91** 057004
- [75] Kaneshita E, Martin I and Bishop A R 2004 Local edge modes in doped cuprates with checkerboard polaronic heterogeneity *Phys. Soc. Japan Lett.* **73** 3223–6
- [76] Nunner T S, Andersen B M, Melikyan A and Hirschfeld P J 2005 Dopant-modulated pair interaction in cuprate superconductors *Phys. Rev. Lett.* **95** 177003
- [77] He Y, Nunner T S, Hirschfeld P J and Cheng H-P 2006 Local electronic structure of $\text{Bi}_2\text{Sr}_2\text{CaCu}_2\text{O}_8$ near oxygen dopants: a window on the high- T_c pairing mechanism *Phys. Rev. Lett.* **96** 197002
- [78] Mori M, Khaliullin G, Tohyama T and Maekawa S 2008 Origin of the spatial variation of the pairing gap in Bi-based high temperature cuprate *Phys. Rev. Lett.* **101** 247003
- [79] Slezak A *et al* 2008 Imaging the impact on cuprate superconductivity of varying the interatomic distances within individual crystal unit cells *Proc. Natl Acad. Sci. USA* **105** 3203–8
- [80] Jinho L *et al* 2006 Interplay of electron-lattice interactions and superconductivity in $\text{Bi}_2\text{Sr}_2\text{CaCu}_2\text{O}_{8+\delta}$ *Nature* **442** 546–50
- [81] Wang Q-H and Lee D-H 2003 Quasiparticle scattering interference in high-temperature superconductors *Phys. Rev. B* **67** 020511
- [82] Capriotti L, Scalapino D J and Sedgewick R D 2003 Wave-vector power spectrum of the local tunneling density of states: ripples in a d -wave sea *Phys. Rev. B* **68** 014508
- [83] Nunner T S, Chen W, Andersen B M, Melikyan A and Hirschfeld P J 2006 Fourier transform spectroscopy of d -wave quasiparticles in the presence of atomic scale pairing disorder *Phys. Rev. B* **73** 104511
- [84] Mesot J *et al* 1999 Superconducting gap anisotropy and quasiparticle interactions: a doping dependent photoemission study *Phys. Rev. Lett.* **83** 840–3
- [85] Chatterjee U *et al* 2006 Nondispersive Fermi arcs and the absence of charge ordering in the pseudogap phase of $\text{Bi}_2\text{Sr}_2\text{CaCu}_2\text{O}_{8+\delta}$ *Phys. Rev. Lett.* **96** 107006
- [86] Chatterjee U *et al* 2007 Anomalous dispersion in the autocorrelation of angle-resolved photoemission spectra of high-temperature $\text{Bi}_2\text{Sr}_2\text{CaCu}_2\text{O}_{8+\delta}$ superconductors *Phys. Rev. B* **76** 012504
- [87] McElroy K *et al* 2006 Elastic scattering susceptibility of the high temperature superconductor $\text{Bi}_2\text{Sr}_2\text{CaCu}_2\text{O}_{8+\delta}$: a comparison between real and momentum space photoemission spectroscopies *Phys. Rev. Lett.* **96** 067005
- [88] Yang K-Y, Rice T M and Zhang F C 2006 Phenomenological theory of the pseudogap state *Phys. Rev. B* **73** 174501
- [89] Corson J, Mallozzi R, Orenstein J, Eckstein J N and Bozovic I 1999 Vanishing of phase coherence in underdoped $\text{Bi}_2\text{Sr}_2\text{CaCu}_2\text{O}_{8+\delta}$ *Nature* **398** 221–3
- [90] Xu Z Z, Ong N P, Wang Y, Kakeshita T and Uchida S 2000 Vortex-like excitations and the onset of superconducting phase fluctuation in underdoped $\text{La}_{2-x}\text{Sr}_x\text{CuO}_4$ *Nature* **406** 486–8
- [91] Wang Y, Li L and Ong N P 2006 Nernst effect in high- T_c superconductors *Phys. Rev. B* **73** 024510
- [92] Wang Y, Li L, Naughton M J, Gu G D, Uchida S and Ong N P 2005 Field-enhanced diamagnetism in the pseudogap state of the cuprate $\text{Bi}_2\text{Sr}_2\text{CaCu}_2\text{O}_{8+\delta}$ superconductor in an intense magnetic field *Phys. Rev. Lett.* **95** 247002
- [93] Li L, Wang Y, Naughton M J, Ono S, Ando Y and Ong N P 2005 Strongly nonlinear magnetization above T_c in $\text{Bi}_2\text{Sr}_2\text{CaCu}_2\text{O}_{8+\delta}$ *Europhys. Lett.* **72** 451–7
- [94] Bergeal N, Lesueur J, Aprili M, Faini G, Contour J P and Leridon B 2008 Pairing fluctuations in the pseudogap state of copper-oxide superconductors probed by the Josephson effect *Nat. Phys.* **4** 608–11
- [95] Pereg-Barnea T and Franz M 2003 Theory of quasiparticle interference patterns in the pseudogap phase of the cuprate superconductors *Phys. Rev. B* **68** 180506
- [96] Misra S, Vershinin M, Phillips P and Yazdani A 2004 Failure of scattering interference in the pseudogap state of cuprate superconductors *Phys. Rev. B* **70** 220503
- [97] Wulin D, He Y, Chien C-C, Morr D K and Levin K 2009 Model for the temperature dependence of the quasiparticle interference pattern in the measured scanning tunnelling spectra of underdoped cuprate superconductors *Phys. Rev. B* **80** 134504

- [98] Kondo T, Khasanov R, Takeuchi T, Schmalian J and Kaminski A 2009 Direct evidence for a competition between the pseudogap and high temperature superconductivity in the cuprates *Nature* **457** 296
- [99] Chen Y, Rice T M and Zhang F C 2006 Rotational symmetry breaking in the ground state of sodium-doped cuprate superconductors *Phys. Rev. Lett.* **97** 237004
- [100] Kaminski A *et al* 2002 Spontaneous breaking of time-reversal symmetry in the pseudogap state of a high- T_c superconductor *Nature* **416** 610–3
- [101] Fauqué B *et al* 2006 Magnetic order in the pseudogap phase of high- T_c superconductors *Phys. Rev. Lett.* **96** 197001
- [102] Li Y *et al* 2008 Unusual magnetic order in the pseudogap region of the superconductor $\text{HgBa}_2\text{CuO}_{4+\delta}$ *Nature* **455** 372–5
- [103] Tranquada J M, Sternlieb B J, Axe J D, Nakamura Y and Uchida S 1995 Evidence for stripe correlations of spins and holes in copper oxide superconductors *Nature* **375** 561–3
- [104] Tranquada J M *et al* 2004 Quantum magnetic excitations from stripes in copper oxide superconductors *Nature* **429** 534–8
- [105] Abbamonte P, Rusydi A, Smadici S, Gu G D, Sawatzky G A and Feng D L 2005 Spatially modulated ‘Mottness’ in $\text{La}_{2-x}\text{Ba}_x\text{CuO}_4$ *Nat. Phys.* **1** 155–68
- [106] Kim Y-J, Gu G D, Gog T and Casa D 2008 X-ray scattering study of charge density waves in $\text{La}_{2-x}\text{Sr}_x\text{CuO}_4$ *Phys. Rev. B* **77** 064520
- [107] Lee W-C, Sinova J, Burkov A A, Joglekar Y and MacDonald A H 2008 Theory of reduced superfluid density in underdoped cuprate superconductors *Phys. Rev. B* **77** 214518
- [108] Graser S, Hirschfeld P J and Scalapino D J 2008 Local quasiparticle lifetimes in a d -wave superconductor *Phys. Rev. B* **77** 184504
- [109] Balents L, Bartosch L, Burkov A, Sachdev S and Sengupta K 2005 Putting competing orders in their place near the Mott transition. II. The doped quantum dimer model *Phys. Rev. B* **71** 144509
- [110] Tešanović Z 2008 d -Wave duality and its reflections in high-temperature superconductors *Nat. Phys.* **4** 408–14
- [111] Vojta M and Rösch O 2008 Superconducting d -wave stripes in cuprates: valence bond order coexisting with nodal quasiparticles *Phys. Rev. B* **77** 094504
- [112] Granath M 2008 Fermi momentum resolved charge order for spin-disordered stripes *Phys. Rev. B* **77** 165128
- [113] Granath M and Andersen B M 2010 Modeling a striped pseudogap state *Phys. Rev. B* **81** 024501
- [114] Bascones E and Valenzuela B 2008 Yang–Rice–Zhang description of checkerboard pattern and autocorrelation of photoemission data in high-temperature superconductors *Phys. Rev. B* **77** 024527